Spectroscopic Definition of the Geometric and Electronic Structure of the Non-Heme Iron Active Site in Iron(II) Bleomycin: Correlation with Oxygen Reactivity

Kelly E. Loeb,[†] Jeffrey M. Zaleski,[†] Tami E. Westre,[†] Richard J. Guajardo,[‡] Pradip K. Mascharak,*[,‡] Britt Hedman,*[,§] Keith O. Hodgson,*[,†,§] and Edward I. Solomon*[,†]

Contribution from the Department of Chemistry and Stanford Synchrotron Radiation Laboratory, Stanford University, Stanford, California 94305, and Department of Chemistry and Biochemistry, University of California, Santa Cruz, California 95064

Received October 28, 1994[⊗]

Abstract: The geometric and electronic structure of high-spin ferrous complexes of bleomycin (Fe^{II}BLM) and the structural analog PMAH ($[Fe^{II}PMA]^+$, where PMAH is a macrocyclic ligand with pyrimidine, imidazole, deprotonated amide, and secondary and primary amine functionalities) have been investigated by optical (Abs) and X-ray (XAS) absorption, magnetic circular dichroism (MCD), and resonance Raman (rR) spectroscopies. From the excited state ligand field transition energies in the low-temperature MCD spectra, the XAS pre-edge shapes and intensities, and EXAFS analysis, solid $[Fe^{II}PMA]^+$ has been determined to have a five-coordinate, square-pyramidal geometry ($E_{d_{x^2-y^2}} - E_{d_{z^2}} = 6100\ cm^{-1}$) with a short Fe–N bond (1.93 Å), while in solution $[Fe^{II}PMA]^+$ binds a solvent molecule at the sixth position to form a distorted octahedral complex ($E_{d_{x^2-y^2}} - E_{d_{z^2}} = 2110\ cm^{-1}$) with an expanded coordination sphere which still maintains one short Fe–N bond (2.00 Å). Similar spectral features consistent with a six-coordinate geometry ($E_{d_{x^2-y^2}} - E_{d_{z^2}} = 2650\ cm^{-1}$) are also present for Fe^{II}BLM in solution, suggesting parallel ligation to the Fe^{2+} center in $[Fe^{II}PMA]^+$ including one relatively short Fe–N bond (2.06–2.08 Å). The magnetic field and temperature dependence of the MCD intensity reveals an unusually small zero-field-splitting of the $S = 2$, $M_s = \pm 2$ non-Kramers doublet ground state of Fe^{II}BLM and $[Fe^{II}PMA]^+$ in solution ($\delta = 2.4\ cm^{-1}$) indicating a large splitting of the d_π orbitals ($E_{d_{xz,yz}} - E_{d_{xy}} = 800$ and 950 cm^{-1}, respectively) resulting from strong metal–ligand π-bonding interactions. The presence of moderately-intense, low-energy metal-to-ligand charge transfer (MLCT) transitions in the low-temperature Abs and MCD spectra of $[Fe^{II}PMA]^+$ and Fe^{II}BLM represents an important deviation from other non-heme iron centers and reflects high covalency. The MLCT transition energies and intensities determine the degree of metal–ligand π-backbonding which decreases along the series solid $[Fe^{II}PMA]^+$ > solution $[Fe^{II}PMA]^+$ > Fe^{II}BLM. Assignment of these bands as iron(II) → pyrimidine MLCT transitions is derived from the strong resonance enhancement of the pyrimidine normal modes at 680, 744, 1519, and 1542 cm^{-1} in the $[Fe^{II}PMA]^+$ Raman spectrum, thereby implicating pyrimidine as the specific ligand associated with the large d_π splitting and short Fe–N bond. This pyrimidine π-backbonding mediates the electron density localized on the Fe^{2+} center which contributes to the unique chemistry of Fe^{II}BLM relative to other non-heme iron sites. This includes its ability to bind π-acceptor exogenous ligands resulting in the conversion to a low-spin state and its formation of a long-lived oxygen intermediate.

Introduction

Bleomycin (BLM) is a histidine-containing glycopeptide antibiotic isolated as a Cu(II) complex from the fungus *Streptomyces verticillus*.[1–3] The drug Blenoxane, composed mainly of BLM A_2, is used in treatment against a variety of carcinomas because of its ability to degrade DNA with sequence specificity.[4] The structure of BLM A_2 (Figure 1a) includes three domains: the bithiazole tail is believed to be involved in BLM binding to DNA,[5–7] the sugar moiety is thought to control uptake of BLM by cancer cells,[8,9] and the β-aminoalanine–pyrimidine–histidine region is responsible for metal chelation.[10,11] DNA degradation by BLM is oxygen and metal ion dependent[12–15] with the greatest enhancement observed for iron.[12,16–21]

[†] Department of Chemistry, Stanford University.
[‡] Department of Chemistry and Biochemistry, University of California, Santa Cruz.
[§] Stanford Synchrotron Radiation Laboratory.
[⊗] Abstract published in *Advance ACS Abstracts*, April 1, 1995.

(1) Umezawa, H.; Maeda, K.; Takeuchi, T.; Oakami, Y. *J. Antibiot.* **1966**, *19*, 200–209.
(2) Umezawa, H.; Surhara, Y.; Takita, T.; Maeda, K. *J. Antibiot.* **1966**, *19*, 210–219.
(3) Umezawa, H. *Biomedicine* **1973**, *18*, 459–475.
(4) Hutchinson, F.; Povirk, L. F. In *Bleomycin: Chemical, Biochemical, and Biological Aspects*; Hecht, S. M., Ed.; Springer-Verlag: New York, 1979; pp 255–266.
(5) Chien, M.; Grollman, A. P.; Horwitz, S. B. *Biochemistry* **1977**, *16*, 3641–3647.
(6) Kross, J.; Henner, W. D.; Haseltine, W. A.; Rodriquez, L.; Levin, M. D.; Hecht, S. M. *Biochemistry* **1982**, *21*, 3711–3721.
(7) Fisher, L. M.; Kuroda, R.; Sakai, T. T. *Biochemistry* **1985**, *24*, 3199–3207.
(8) Umezawa, H. *Pure Appl. Chem.* **1971**, *28*, 665–680.
(9) DeReimer, L. H.; Meares, C. F.; Goodwin, D. A.; Diamanti, C. I. *J. Med. Chem.* **1979**, *22*, 1019–1023.
(10) Stubbe, J.; Kozarich, J. W. *Chem. Rev.* **1987**, *87*, 1107–1136.
(11) Petering, D. H.; Byrnes, R. W.; Antholine, W. E. *Chem.-Biol. Interact.* **1990**, *73*, 133–182.
(12) Sausville, E. A.; Peisach, J.; Horwitz, S. B. *Biochemistry* **1978**, *17*, 2740–2746.
(13) Ishida, R.; Takahashi, T. *Biochem. Biophys. Res. Commun.* **1975**, *66*, 1432–1438.
(14) Oppenheimer, N. J.; Chang, C.; Rodriguez, L. O.; Hecht, S. M. *J. Biol. Chem.* **1981**, *256*, 1514–1517.

0002-7863/95/1517-4545$09.00/0

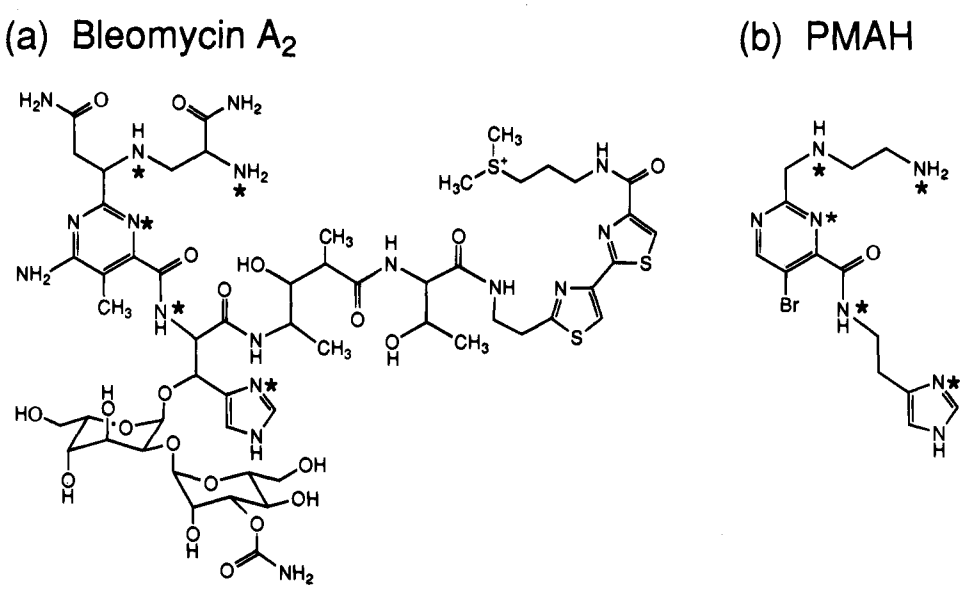

Figure 1. Structural ligand framework of (a) Bleomycin A_2 and (b) the analogous model complex PMAH. Coordinating nitrogens are denoted with asterisks (*) for each structure.

Oxygen binds to Fe^{II}BLM producing a ternary complex (oxygenated BLM) that is stable in the presence of excess DNA.[22-24] Transfer of an additional electron from a second Fe^{II}BLM molecule (or other reductant) to oxygenated BLM produces activated BLM, the species responsible for DNA strand scission.[25] The similarity in mechanism to cytochrome P-450 has led researchers to postulate a ferryl (Fe^{IV}=O) BLM intermediate,[10,19] as has generally been considered to be present in heme chemistry.[26] Alternatively, electron paramagnetic resonance (EPR),[19] Mössbauer,[24] mass spectrometry,[27] and X-ray absorption spectroscopy (XAS)[28] of activated BLM are most consistent with a low-spin iron(III) peroxide site.

No crystal structure exists for the ferrous complex of BLM and there is some controversy concerning the ligation of BLM to Fe^{2+}. Present descriptions are based on correlations to a Cu(II) complex of the related biosynthetic precursor P-3A, which has been crystallographically defined and shown to have a five-coordinate, square-pyramidal geometry with pyrimidine, imidazole, deprotonated amide, and secondary amine functions forming the equatorial plane and a primary amine function coordinating axially.[29] However, Cu^{2+} has strong structural preferences due to the Jahn-Teller effect which Fe^{2+} does not and P-3A lacks the dissacharide and bithiazole moieties of BLM, the former being a potential ligand. Axial coordination in Fe^{II}-BLM of the carbamoyl group of the mannose sugar has been implicated by ^{1}H nuclear magnetic resonance (NMR) studies[30-32] and two-dimensional NMR studies of the carbon monoxide bound form.[33] In contrast, earlier studies of CO-bound Fe^{II}-BLM maintained axial coordination of the primary amine and proposed that the sugar portion played a steric role in governing CO binding constants via hydrogen bonding to the β-amino-propionamide group.[34] EPR spectroscopy on the nitrosyl complex of Fe^{II}BLM has been used to further support the model that the axial donor *trans* to the bound NO is the primary nitrogen of the α-amino group of the β-aminoalanine portion.[35-37] Additional evidence for axial coordination of the primary amine derives from the variation in EPR parameters for Fe^{III}BLM and the ferric complexes of depyruvamide BLM and deamido BLM.[38]

There is little direct spectroscopic evidence available on Fe^{II}-BLM as the Mössbauer spectra exhibit broad, unresolved magnetic features and high-spin Fe^{2+} non-Kramers ions generally do not exhibit EPR signals.[24] As a result, most experiments have focused on the spectroscopically accessible ferric forms of the drug. We have developed an effective probe of mononuclear non-heme ferrous active sites using a combination of absorption (Abs), circular dichroism (CD), and magnetic circular dichroism (MCD) to observe ligand field excited states in the near-infrared (NIR) spectral region and variable-temperature variable-field (VTVH) MCD to obtain ground state

(15) Ehrenfeld, G. M.; Murugesan, N.; Hecht, S. M. *Inorg. Chem.* **1984**, *23*, 1496-1498.
(16) Lown, J. W.; Sim, S.-K. *Biochem. Biophys. Res. Commun.* **1977**, *77*, 1150-1157.
(17) Sausville, E. A.; Peisach, J.; Horwitz, S. B. *Biochem. Biophys. Res. Commun.* **1976**, *73*, 814-822.
(18) Sausville, E. A.; Stein, R. W.; Peisach, J.; Horwitz, S. B. *Biochemistry* **1978**, *17*, 2746-2754.
(19) Burger, R. M.; Peisach, J.; Horwitz, S. B. *J. Biol. Chem.* **1981**, *256*, 11636-11644.
(20) Giloni, L.; Takeshita, M.; Johnson, F.; Iden, C.; Grollman, A. P. *J. Biol. Chem.* **1981**, *256*, 8608-8615.
(21) Burger, R. M.; Berkowitz, A. R.; Peisach, J.; Horwitz, S. B. *J. Biol. Chem.* **1980**, *255*, 11832-11838.
(22) Fulmer, P.; Petering, D. H. *Biochemistry* **1994**, *33*, 5319-5327.
(23) Albertini, J.-P.; Gamier-Suillerot, A.; Tosi, L. *Biochem. Biophys. Res. Commun.* **1982**, *104*, 557-563.
(24) Burger, R. M.; Kent, T. A.; Horwitz, S. B.; Münck, E.; Peisach, J. *J. Biol. Chem.* **1983**, *258*, 1559-1564.
(25) Hecht, S. M. *Acc. Chem. Res.* **1986**, *19*, 383-391.
(26) Ortiz de Montellano, P. R. *Cytochrome P-450: Structure, Mechanism, and Biochemistry*; Plenum Press: New York, 1986; pp 429-503.
(27) Sam, J. W.; Tang, X.-J.; Peisach, J. *J. Am. Chem. Soc.* **1994**, *116*, 5250-5256.
(28) Westre, T. E.; Loeb, K. E.; Zaleski, J. M.; Hedman, B.; Hodgson, K. O.; Solomon, E. I. *J. Am. Chem. Soc.* **1995**, *117*, 1309-1313.
(29) Iitaka, Y.; Nakamura, H.; Nakatani, T.; Muraoka, Y.; Fujii, A.; Takita, T.; Umezawa, H. *J. Antibiot.* **1978**, *31*, 1070-1072.
(30) Sugiura, Y.; Suzuki, T.; Otsuka, M.; Kobayashi, S.; Ohno, M.; Takita, T.; Umezawa, H. *J. Biol. Chem.* **1983**, *258*, 1328-1336.
(31) Oppenheimer, N. J.; Chang, C.; Chang, L.-H.; Ehrenfeld, G.; Rodriguez, L. O.; Hecht, S. M. *J. Biol. Chem.* **1982**, *257*, 1606-1609.
(32) Oppenheimer, N. J.; Rodriguez, L. O.; Hecht, S. M. *Proc. Natl. Acad. Sci. U.S.A.* **1979**, *76*, 5616-5620.
(33) Akkerman, M. A. J.; Neijman, E. W. J. F.; Wijmenga, S. S.; Hilbers, C. W.; Bermel, W. *J. Am. Chem. Soc.* **1990**, *112*, 7462-7474.
(34) Sugiura, Y.; Kuwahara, J.; Suzuki, T. *FEBS Lett.* **1985**, *182*, 39-42.
(35) Sugiura, Y.; Ishizu, K. *J. Inorg. Biochem.* **1979**, *11*, 171-180.
(36) Sugiura, Y. *J. Antibiot.* **1978**, *31*, 1206-1208.
(37) Sugiura, Y.; Ishizu, K.; Miyoshi, K. *J. Antibiot.* **1979**, *32*, 453-461.
(38) Sugiura, Y. *J. Am. Chem. Soc.* **1980**, *102*, 5208-5215.

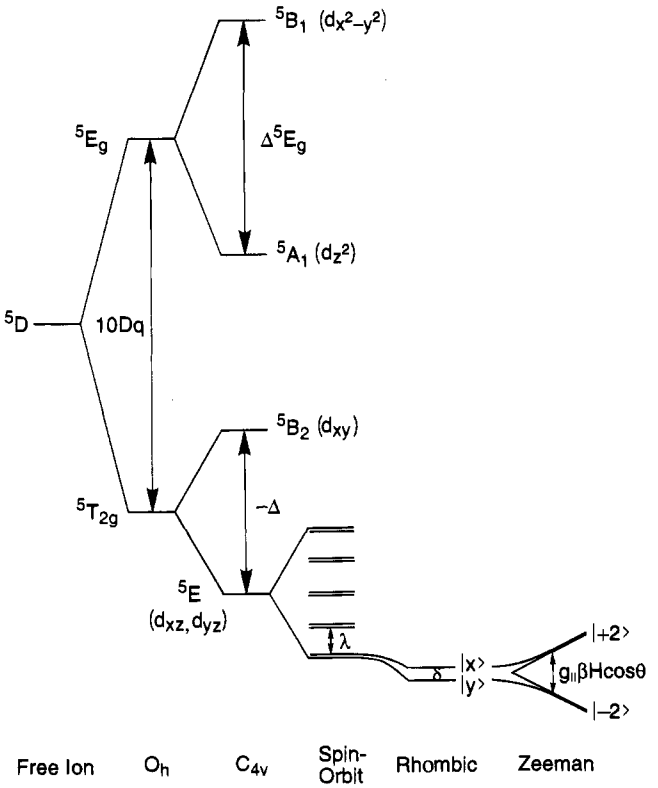

Figure 2. The $^5T_{2g}$ ground state and ^5E_g excited state splitting patterns following descent in symmetry from an octahedral field. Removal of an axial ligand splits the ^5E_g excited state by an energy of Δ^5E_g into $^5B_1$ and $^5A_1$ states derived from one-electron transitions to the $d_{x^2-y^2}$ and d_{z^2} orbitals, respectively. Similarly, the $^5T_{2g}$ state is split by $-\Delta$ into $^5B_2$ (d_{xy}) and ^5E ($d_{xz,yz}$) states. In-state spin–orbit coupling splits the ^5E_g state into a manifold of five doublets separated by λ. A rhombic distortion V splits the d_{xz} and d_{yz} orbitals and lifts the degeneracy of the lowest doublet by an amount δ resulting in real wave functions $|x\rangle$ and $|y\rangle$ in zero magnetic field which are linear combinations of the non-Kramers $M_s = \pm 2$ levels. These states become purely complex ($|+2\rangle$ and $|-2\rangle$) at high magnetic fields, resulting in MCD intensity that increases with increasing field and decreasing temperature.

sublevel splittings.[39,40] For a high-spin d^6 ferrous ion, the free ion term symbol is ^5D, which splits into $^5T_{2g}$ and ^5E_g orbital states in an octahedral field as shown in Figure 2. For biologically relevant ligands such as N or O, the splitting $10Dq$ is on the order of 10 000 cm^{-1}. Low-symmetry distortions (or a Jahn–Teller interaction in octahedral symmetry) split the ^5E_g state by $\Delta^5E_g \approx 2000$ cm^{-1} into $^5B_1$ and $^5A_1$ levels. Complete removal of one axial ligand causes a larger splitting, $\Delta^5E_g \approx 5000$ cm^{-1}. Transitions to these excited states are not often observed by optical absorption since they are relatively weak (parity forbidden) and in the region of ligand and buffer vibrations, but they can be readily observed in CD and MCD spectroscopy due to differences in selection rules. In less than octahedral symmetry there will also be an axial splitting of the $^5T_{2g}$ ground level into $^5B_2$ and ^5E states (Figure 2) by an amount $-\Delta$ reflecting differences in the π ligand field splitting of the t_{2g} orbitals ($E_{d_{xz,yz}} - E_{d_{xy}}$). For weak axial distortions from octahedral symmetry, as is often observed in coordination complexes, the orbitally degenerate ^5E state (d_{xz} and d_{yz} orbitals) is lowest in energy corresponding to $\Delta < 0$. Allowing for in-state spin–orbit coupling within the ^5E state and neglecting the minimal contributions from spin–orbit interactions with higher energy states produces a manifold of five doublets separated by λ. The many-electron spin–orbit coupling parameter λ is equal to -100 cm^{-1} for the Fe^{2+} free ion but is reduced to ~ -80 cm^{-1} due to covalency effects upon complexation. A rhombic distortion of magnitude V (the energy splitting of the d_{xz} and d_{yz} orbitals) splits the spin–orbit perturbed ^5E ground state and leaves a non-Kramers doublet lowest in energy split by an amount δ. Application of an external magnetic field causes an additional splitting of these sublevels and changes the mixing of their wave functions. These states are real in zero magnetic field ($|x\rangle$ and $|y\rangle$ in Figure 2 which are normalized linear combinations of the $M_s = \pm 2$ levels) and purely complex ($|+2\rangle$ and $|-2\rangle$) at high magnetic fields. MCD intensity requires pure complex character which increases with increasing field and decreasing temperature, leveling off at the high-field, low-temperature limit. The field and temperature dependence of the MCD intensity (called saturation magnetization curves) can then be used to estimate the values of δ, the splitting of the lowest energy non-Kramers doublet, and $g_{||}$, the magnitude of the Zeeman splitting with the applied magnetic field parallel to the z-axis. The experimentally determined δ and $g_{||}$ can then be related to Δ and V (the ligand field splittings of the $^5T_{2g}$ state) by using Figure 13 in ref 40.[41] It should be noted that this ligand field model relates to the pure spin Hamiltonian description with $D < 0$ corresponding to a degenerate $M_s = \pm 2$ non-Kramers doublet ground state but allows for an additional orbital angular momentum contribution to the ground state splittings. Determination of the ground and excited state energy splittings reveals vital geometric and electronic structural information regarding the ligand field environment about the metal center which can be used to gain insight into O_2 reactivity.

We have applied the above protocol to $Fe^{II}BLM$ and have quantitatively defined the excited state ^5E_g and the ground state $^5T_{2g}$ splittings and therefore the relative energies of the d-orbitals which provide a foundation for understanding the geometric and electronic structure of $Fe^{II}BLM$. We have further characterized the coordination number and bond lengths of $Fe^{II}BLM$ using XAS. Due to the complexity of the glycopeptide and the range of possible metal coordinating functional groups in BLM, synthetic models have been prepared in an effort to obtain insight into the structure.[43–49] We have also investigated the synthetic analog PMAH[50] which has a similar metal binding domain but lacks the sugar moiety and the bithiazole tail (Figure 1b). The ferrous complex serves as a good model of $Fe^{II}BLM$ in that it reacts with dioxygen to generate an analog of activated BLM which has a nearly identical EPR spectrum and causes DNA cleavage with similar specificity.[43] $Fe^{II}BLM$ (and $[Fe^{II}PMA]^+$) is a member of a series of non-heme Fe sites that

(39) Whittaker, J. W.; Solomon, E. I. *J. Am. Chem. Soc.* **1986**, *108*, 835–836.
(40) Whittaker, J. W.; Solomon, E. I. *J. Am. Chem. Soc.* **1988**, *110*, 5329–5339.
(41) Note that updated versions of these plots to indicate small differences in $g_{||}$ values are given in ref 42.
(42) Solomon, E. I.; Pavel, E. G.; Loeb, K. E.; Campochiaro, C. *Coord. Chem. Rev.* In press.
(43) Guajardo, R. J.; Hudson, S. E.; Brown, S. J.; Mascharak, P. K. *J. Am. Chem. Soc.* **1993**, *115*, 7971–7977.
(44) Henichart, J.-P.; Bernier, J.-L.; Helbecque, N.; Houssin, R. *Nucl. Acid Res.* **1985**, *13*, 6703–6717.
(45) Kenani, A.; Bailly, C.; Helbecque, N.; Houssin, R.; Bernier, J.-L.; Henichart, J.-P. *Eur. J. Med. Chem.* **1989**, *24*, 371–377.
(46) Sugiyama, T.; Ohno, M.; Shibasaki, M.; Otsuka, M.; Suglura, Y.; Kobayashi, S.; Maeda, K. *Heterocycles* **1994**, *37*, 275–282.
(47) Shepherd, R. E.; Lomis, T. J.; Koepsel, R. R.; Hedge, R.; Mistry, J. S. *Inorg. Chim. Acta* **1990**, *171*, 139–149.
(48) Brown, S. J.; Tao, X.; Wark, T. A.; Stephan, D. W.; Mascharak, P. K. *Inorg. Chem.* **1988**, *27*, 1581–1587.
(49) Muettertjes, M.; Mascharak, P. K.; Cox, M. B.; Arora, S. K. *Inorg. Chim. Acta* **1989**, *160*, 123–134.
(50) PMAH is 2-((*N*-(aminoethyl)amino)methyl)-4-(*N*-(2-(4-imidazolyl)-ethyl)carbamoyl)-5-bromopyrimidine where H is the dissociable amide proton. PMAH forms a 1:1 iron complex with pyrimidine, imidazole, amide, and secondary and primary amine functionalities.

activate O_2 from the Fe^{2+} oxidation state which include the extradiol dioxygenases, pterin hydroxylases, α-ketoglutarate dioxygenases, *etc.* However, the active sites in Fe^{II}BLM and $[Fe^{II}PMA]^+$ are very unusual relative to the other non-heme Fe systems in that they possess low-energy charge transfer (CT) transitions in the 350−750-nm region. We have also studied these CT transitions using low-temperature Abs and MCD and elucidated their origin through resonance Raman (rR) profiles of $[Fe^{II}PMA]^+$ based on a vibrational assignment derived from the spectra of a series of derivatives, $[Fe^{II}(Prpep)_2]$, $[Fe^{II}(Pypep)_2]$, and $[Fe^{II}PMD]^+$, where the metal-binding ligand framework (coordinating nitrogens are denoted with asterisks) has been systematically perturbed.[51]

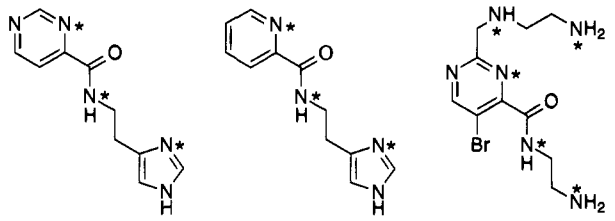

From these studies, the transitions involve iron(II) → pyrimidine CT and provide a direct reflection of π-backbonding into the pyrimidine which can greatly influence the chemistry and reactivity of this complex relative to other non-heme Fe sites, as is described in the last section of this paper.

Experimental Section

Bleomycin sulfate (Blenoxane), a mixture of 60% BLM A_2, 30% BLM B_2, and 10% other BLM fractions, was obtained as a gift from Bristol-Meyers Squibb and used without further purification. The individual components differ only in the terminal amine functionality which has no influence on the spectroscopic characteristics of the metal-binding domain.[19] All concentrations were calculated with a molecular weight of ~1510 daltons. Low-temperature Abs, CD, MCD, and XAS Fe^{II}BLM samples were prepared as glasses in 50% (v/v) glycerol-d_3 (98 atom % D; Aldrich) or ethylene glycol-d_2 (98 atom % D; Aldrich)/300 mM HEPES buffer (Sigma) dissolved in D_2O (99.9 atom % D; Aldrich) and adjusted to a pD in the range 6.0−9.0 with 40 wt % NaOD (Aldrich) in D_2O. Septum stoppered reaction flasks were not sufficient to prevent O_2 reaction; therefore, all solutions were rigorously degassed with 10−15 freeze−pump−thaw cycles at 10^{-5} Torr in Teflon or ground glass stoppered flasks and immediately placed in a N_2 atmosphere (<10 ppm of O_2). Solid forms of metal free BLM and $Fe(NH_4)_2(SO_4)_2{\cdot}6H_2O$ (FeAS; MCB Manufacturing Chemists, Inc.) were solvated just prior to use in an inert atmosphere with buffered solution and D_2O, respectively. Fe^{II}BLM was prepared in the presence of 20% excess ligand by addition of 5 μL of the FeAS stock solution to 5 mM metal free BLM to give a final sample concentration of ~4 mM. Sample integrity was confirmed by optical Abs ($\epsilon_{476} = 380\ M^{-1}\ cm^{-1}$)[18] and EPR. The use of reducing agents to inhibit Fe^{2+} oxidation was strictly avoided as it was determined to significantly alter both the CD and MCD spectra of Fe^{II}BLM. Solid samples of Fe^{II}BLM were achieved by lyophilization of 400 μL of 20 mM Fe^{II}BLM in 300 mM, pD = 7.0 HEPES buffer.

The ligands PypepH,[52] PrpepH,[49] and PMAH,[53] were synthesized according to published procedures, followed by anaerobic complexation with Fe^{2+} to form $[Fe^{II}(Pypep)_2]{\cdot}2CH_3OH$,[54] $[Fe^{II}(Prpep)_2]{\cdot}2CH_3OH$,[55] $[Fe^{II}(PMA)]Cl{\cdot}MeOH$,[43] and $[Fe^{II}(PMA)]I{\cdot}MeOH$.[54] $[Fe^{II}PMD]^+$ was prepared *in situ* by direct complexation of 1 equiv of $FeCl_2{\cdot}2H_2O$ with a slight excess of PMDH in methanol.[54] Samples of $[Fe^{II}(Pypep)_2]$, $[Fe^{II}(Prpep)_2]$, and $[Fe^{II}PMA]^+$ for room temperature Abs and rR were prepared by dissolving the solids in methanol (reagent grade, Baker) which had been refluxed for 30 min, distilled over CaH_2, initially dried for 24 h, and subsequently stored over 3 Å molecular sieves. $[Fe^{II}PMA]^+$ solutions for low-temperature Abs, MCD, and XAS were prepared in a N_2 atmosphere with degassed methanol-d_4 (99.9 atom % D; Aldrich) and ethanol-d_6 (99+ atom % D; Aldrich) in a ratio of 1 to 4 to facilitate glassing. Sample concentrations were determined by optical absorption ($\epsilon_{592}([Fe^{II}(Pypep)_2]) = 2915\ M^{-1}\ cm^{-1}$,[54] $\epsilon_{670}([Fe^{II}(Prpep)_2]) = 5300\ M^{-1}\ cm^{-1}$,[55] $\epsilon_{673}([Fe^{II}PMD]^+) = 1880\ M^{-1}\ cm^{-1}$,[54] and $\epsilon_{670}([Fe^{II}PMA]^+) = 1850\ M^{-1}\ cm^{-1}$) to be ~20 mM for rR, ~1−2 mM for low-temperature Abs and MCD, and ~4 mM for XAS.

Room temperature UV/vis optical Abs spectra (190−820 nm) were recorded on an HP 8452A diode array or a Perkin-Elmer Lambda 9 spectrophotometer. Air-sensitive samples were syringed into a 1 mm path length cuvette adapted with a Kontes Teflon stopcock because septum stoppered cuvettes used without precautionary reducing agents were not sufficient to prevent air oxidation of the ferrous samples. Low-temperature UV/vis absorption spectra (8 K, 300−900 nm) were recorded on a Cary 17 UV/vis spectrophotometer equipped with a Janis Super Varitemp helium cryostat and interfaced to a Compaq 386 computer with OLIS software. Residual absorption due to solvent, buffer, or glass scattering effects was subtracted from all of the spectra. For low-temperature Abs (and MCD) experiments, the sample was injected into a cell assembled under N_2 with a neoprene spacer (3 mm path length, 6 mm i.d., 12 mm o.d.) sandwiched between two infrasil quartz disks. The sample was kept anaerobic until insertion into the cryostat under a flow of He gas. Low-temperature UV/vis CD and MCD spectra (1.6−50 K, 300−850 nm) were obtained on a Jasco J500C spectropolarimeter with an extended S-20 photomultiplier tube (Hammamatsu), interfaced to an IBM XT computer, and equipped with an Oxford SM4-6T magnet/cryostat. Depolarization of frozen samples (<10%) for all low-temperature CD and MCD experiments was measured by monitoring the CD intensity of a nickel (+)-tartrate solution placed before and after the sample.[56] Solid state MCD spectra were obtained by addition of ~200 μL of fluorolube mulling agent (Wilmad) to finely ground solid Fe^{II}BLM and $[Fe^{II}PMA]^+$ followed by compression of the suspension between two infrasil quartz disks. Room temperature NIR CD spectra (278 K, 600−2000 nm) were obtained using a Jasco 200D spectropolarimeter interfaced to a Macintosh IIvx computer and a LN_2-cooled InSb detector. Data acquisition was achieved using routines written within the software package LabVIEW (National Instruments). Samples were placed in a 1 cm path length NIR cuvette equipped with a Kontes stopcock and cooled by a recirculating water bath. Low-temperature NIR CD and MCD spectra (1.6−150 K, 600−2150 nm) were obtained with the Jasco 200D spectropolarimeter and an Oxford SM4-7T magnet/cryostat. Abs, CD, and MCD spectra were smoothed using a weighted fitting routine and simultaneously fit to Gaussian bandshapes using a constrained nonlinear least-squares fitting procedure.

Room temperature rR spectra (600−1800 cm^{-1}) were obtained using a SPEX 1403 double monochromator with a cooled Burle C31034-02 photomultiplier tube operated with a SPEX digital photometer (DPC-2) interfaced to a Compaq 286 computer. Sample illumination with 5−100 mW of laser power was performed in a 150° backscattering geometry with a Coherent I-90K Kr^+ or I-18UV Ar^+ ion laser, or an Ar^+-pumped (6 W at 514.5 nm) Coherent 590 dye laser using R590, R640, or DCM Special dyes (Exciton) at ~2 mM concentrations in a 1:9 ratio of methanol−ethylene glycol (Mallinckrodt). Solution samples were prepared under a N_2 atmosphere in 528-PP quartz NMR tubes containing a Teflon J. Young valve (Wilmad Glass) and were placed

(51) PrpepH is *N*-(2-(4-imidazolyl)ethyl)pyrimidine-4-carboxamide, PypepH is *N*-(2-(4-imidazolyl)ethyl)pyridine-2-carboxamide, and PMDH is 2-((*N*-(aminoethyl)amino)methyl)-4-(*N*-(2-aminoethyl)carbamoyl)-5-bromopyrimidine, where H is the dissociable amide proton. $[Fe^{II}(Prpep)_2]$ and $[Fe^{II}(Pypep)_2]$ are *bis*-complexes of a tridentate ligand with the same histidine and deprotonated amide functionalities and differ only in the exchange of pyrimidine (Pm) with pyridine (Py), respectively. $[Fe^{II}PMD]^+$ is a 1:1 complex with the same structure as $[Fe^{II}PMA]^+$ except for replacement of the imidazole with an NH_2 group.

(52) Brown, S. J.; Tao, X.; Stephan, D. W.; Mascharak, P. K. *Inorg. Chem.* **1986**, *25*, 3377−3384.

(53) Brown, S. J.; Mascharak, P. K.; Stephan, D. W. *J. Am. Chem. Soc.* **1988**, *110*, 1996−1997.

(54) Guajardo, R. J.; Mascharak, P. K. Unpublished results.

(55) Brown, S. J.; Olmstead, M. M.; Mascharak, P. K. *Inorg. Chem.* **1990**, *29*, 3229−3234.

(56) Browett, W. R.; Fucaloro, A. F.; Morgan, T. V.; Stephens, P. J. *J. Am. Chem. Soc.* **1983**, *105*, 1868−1872.

in a gas-driven NMR tube spinner. Samples were determined to be stable from photodegradation and oxidation over the timecourse of several scans. Typically, 1−3 scans were accumulated, each obtained in 2-cm^{-1} increments with an integration time of 5 s per point and 300−500-μm slits. For the resonance enhancement profile, the 1034-cm^{-1} Raman band of the methanol solvent was used as an internal standard. Deuterated samples of $[Fe^{II}PMA]^+$ and $[Fe^{II}PMD]^+$ were prepared by dissolving the solid complex in methanol-d_4 and stirring for 15 min prior to the Raman experiment.

X-ray absorption spectra were recorded at the Stanford Synchrotron Radiation Laboratory (SSRL) on unfocused beamline 7−3 during dedicated conditions (3 GeV, 50−100 mA). The radiation was monochromatized using a Si(220) double-crystal monochromator. Unless specified otherwise, data were measured to $k = 15$ Å^{-1} with 1 mm high pre-monochromator beam defining slits and the monochromator was detuned by 50% at 7998 eV to minimize harmonic contamination. An Oxford Instruments continuous-flow liquid helium CF1208 cryostat was used to maintain a constant temperature of 10 K. Energies were calibrated using an internal Fe foil standard, assigning the first inflection point to 7111.2 eV.[57] The spectrometer energy resolution was ~1.5 eV with reproducibility in edge position determination of <0.2 eV.

The $[Fe^{II}PMA]^+$ solution and $Fe^{II}BLM$ XAS samples were prepared as described above. The solution samples were syringed into Lucite EXAFS cells (23 × 1 × 3 mm^3) with 37 μm Kapton windows under a N_2 atmosphere and subsequently frozen in liquid nitrogen prior to exposure to air. The fluorescence signal was monitored by using a 13-element Ge solid-state array detector[58] windowed on the Fe Kα signal. During the experiment, count rates of approximately 30 000 s^{-1} total per element were not exceeded. Approximatly 30 scans were averaged for $Fe^{II}BLM$ and 11 scans were averaged for the $[Fe^{II}PMA]^+$ solution. The powder $[Fe^{II}PMA]^+$ sample was mixed with BN and ground into a fine powder in a N_2-filled glovebox. This BN/sample mixture was pressed into a 1 mm thick Al spacer that was sealed with 63.5 μm Mylar tape windows and frozen in liquid nitrogen. Data were measured in transmission mode with N_2-filled ionization chambers. The final spectrum represents a 6-scan average.

EXAFS data reduction was performed on the averaged spectra according to established methods.[59−61] A smooth pre-edge background was removed from the averaged spectra by fitting a second-order polynomial to the pre-edge region and subtracting this polynomial from the entire spectrum. A three-segment spline approximately even in k-space was fit to the EXAFS region and the data normalized to an edge jump of one at 7130 eV. The spline was chosen so that it minimized residual low-frequency background but did not reduce the EXAFS amplitude as checked by monitoring the Fourier transform of the EXAFS during the background subtraction process. The normalized data were converted to k-space. The photoelectron wave vector, k, is defined by $[2m_e(E - E_0)/\hbar^2]^{1/2}$, where m_e is the electron mass, E is the photon energy, $\hbar$ is Planck's constant divided by 2π, and E_0 is the threshold energy of the absorption edge, which was defined to be 7130 eV for the Fe K absorption edge. The empirical EXAFS data analyses were performed with nonlinear least-squares curve-fitting[57,59−61] techniques using empirical phase and amplitude parameters. The following models were used to obtain the empirical Fe−X backscattering parameters of interest: Fe−O from $[Fe(acetylacetonate)_3]$[62,63] and Fe−N from $[Fe(1,10\text{-phenanthroline})_3](ClO_4)_3$.[64,65] Fourier transforms (from k- to R-space) were performed for the data range 3.5−12.5 Å^{-1} with a Gaussian window of 0.1 Å^{-1}. The window widths used in the backtransforms (from R- to k-space) are given in the results section. The window widths were kept as similar as possible to those used to extract amplitude and phase parameters from the model compounds to minimize artifacts introduced by the Fourier filtering technique. All curve-fitting was based on k^3-weighted data and applied to the individual filtered shell of interest. Only the structure-dependent parameters, the distance and coordination number, were varied unless stated otherwise. A "goodness of fit" parameter, F, was calculated as $F = \{[k^6(\text{data} - \text{fit})^2]/(\text{no. of points})\}^{1/2}$ for each fit.

Fe K-edge spectra were also collected on a five- and a six-coordinate ferrous model complex. $[Fe(TMC)N_3]BF_4$[66] (where TMC refers to tetramethylcyclam) and $[Fe(imidazole)_6]Cl_2$[67] were prepared as previously described. The XAS samples were prepared in the same manner as the $[Fe^{II}PMA]^+$ solid sample. Data were measured in transmission mode with N_2-filled ionization chambers to $k = 9.5$ Å^{-1} detuning the monochromator 50% at 7474 eV to minimize harmonic contamination. Two to three scans were averaged for each sample. A smooth pre-edge background was removed from the averaged spectra by fitting a first-order polynomial to the pre-edge region and subtracting this polynomial from the entire spectrum. A two-segment spline of order two was fit to the EXAFS region and the data normalized to an edge jump of one at 7130 eV.

Results and Analysis

A. Absorption/Circular Dichroism/Magnetic Circular Dichroism. The room temperature CD and low-temperature Abs and MCD spectra of $Fe^{II}BLM$ from ~5 000 to ~30 000 cm^{-1} are shown in Figure 3. The optical spectrum exhibits weak Abs intensity in the ligand field region below 15 000 cm^{-1}, but d → d bands are clearly present in the CD and low-temperature MCD spectra around 10 000 cm^{-1}. Above 15 000 cm^{-1} two moderately intense CT envelopes are observed in the Abs spectrum near 20 000 and 26 000 cm^{-1} with significant differences in the CD and MCD spectra in this region. The low-temperature Abs and MCD spectra of $[Fe^{II}PMA]^+$ in solution and the MCD spectrum of $[Fe^{II}PMA]^+$ solid are displayed in Figure 4 in the same energy region. In the ligand field region, both MCD spectra exhibit two d → d bands with different splittings indicative of a change in coordination number. In the CT region, the optical spectrum shows two maxima at 15 000 and 20 000 cm^{-1} while the MCD intensity of $[Fe^{II}PMA]^+$ in solution is greatest at 18 000 cm^{-1} with each of the three envelopes comprised of overlapping features. The MCD spectrum of solid $[Fe^{II}PMA]^+$ shows a red shift from the solution of ~2000 cm^{-1}.

1. Ligand Field Region. The ligand field CD spectrum of $Fe^{II}BLM$ is expanded in Figure 5a revealing two transitions which can be fit to Gaussian bandshapes with maxima at 9 100 and 13 050 cm^{-1}. Since the uncomplexed apo-ligand in solution exhibits no CD intensity in this energy region the bands are assigned as Fe^{2+} d → d ligand field transitions corresponding to promotion of an electron to the d_{z^2} and $d_{x^2-y^2}$ orbitals, respectively, which have a ^5E_g orbital state splitting, Δ^5E_g in Figure 2, of 3950 cm^{-1}. The energies and bandshapes of these transitions are independent of pD between 6.0 and 9.0 and unaffected by the addition of the glassing agents glycerol or ethylene glycol. This splitting of almost 4000 cm^{-1} is in between six- and five-coordination and consistent with a weak axial ligand in solution. Upon cooling to 1.6 K, the CD bands of the $Fe^{II}BLM$ solution show a reduced Δ^5E_g splitting attributed to a limited temperature dependent geometric distortion at the Fe^{2+} site. The MCD spectra of $Fe^{II}BLM$ shown in Figure 5b exhibit two Gaussian resolved features at 9 400 and 12 050 cm^{-1}, giving $\Delta^5E_g \approx 2650$ cm^{-1}, consistent with a six-

(57) Scott, R. A.; Hahn, J. E.; Doniach, S.; Freeman, H. C.; Hodgson, K. O. *J. Am. Chem. Soc.* **1982**, *104*, 5364−5369.
(58) Cramer, S. P.; Tench, O.; Yocum, M.; George, G. N. *Nucl. Instrum. Methods Phys. Res.* **1988**, *A266*, 586−591.
(59) Cramer, S. P.; Hodgson, K. O.; Stiefel, E. I.; Newton, W. E. *J. Am. Chem. Soc.* **1978**, *100*, 2748−2761.
(60) Cramer, S. P.; Hodgson, K. O. *Prog. Inorg. Chem.* **1979**, *25*, 1−39.
(61) Scott, R. A. *Methods Enzymol.* **1985**, *117*, 414−459.
(62) Iball, J.; Morgan, C. H. *Acta Crystallogr.* **1967**, *23*, 239−244.
(63) Roof, R. B., Jr. *Acta Crystallogr.* **1956**, *9*, 781−786.
(64) Johansson, L.; Molund, M.; Oskarsson, Å. *Inorg. Chim. Acta* **1978**, *31*, 117−123.
(65) Johansson, L. *Chem. Scr.* **1976**, *9*, 30−35.
(66) Hodges, K. D.; Wollman, R. G.; Barefield, E. K.; Hendrickson, D. N. *Inorg. Chem.* **1977**, *16*, 2746−2751.
(67) Burbridge, C. D.; Goodgame, D. M. L. *Inorg. Chim. Acta* **1970**, *4*, 231−234.

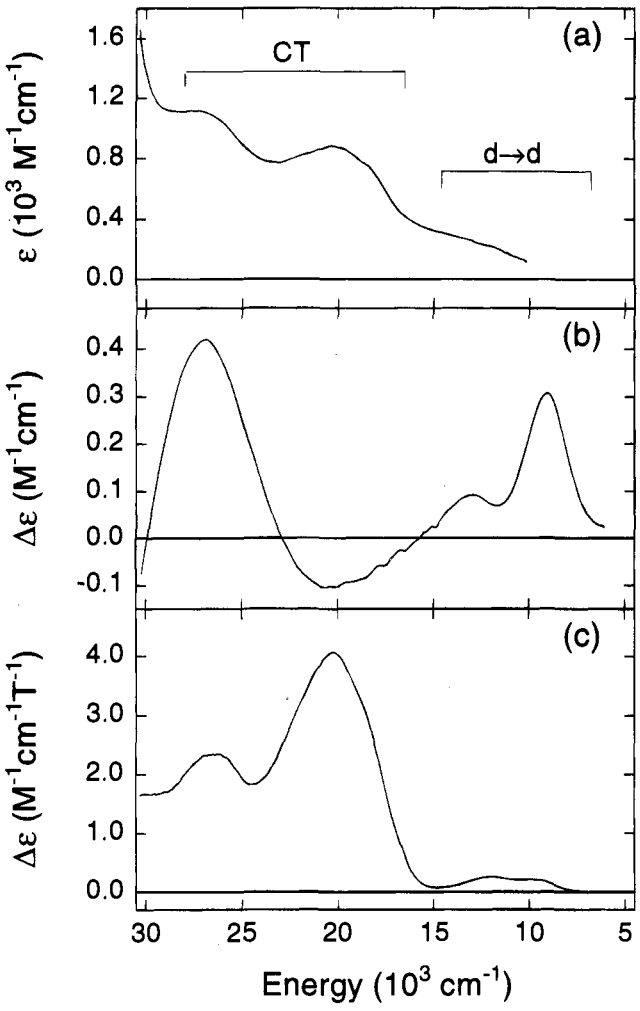

Figure 3. Spectral features of Fe^{II}BLM in HEPES buffer/glycerol, pD 7.0 between 5 000 and 30 000 cm^{-1}: (a) Abs spectrum at 8 K; (b) CD spectrum at 278 K; (c) MCD spectrum at 5 K and 6 T.

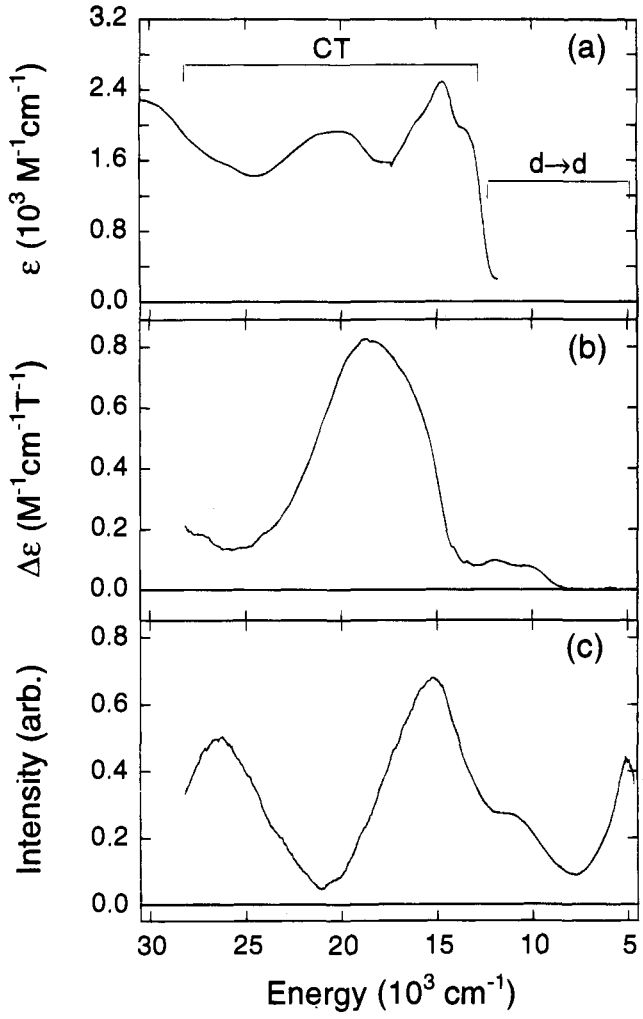

Figure 4. Spectral features of $[Fe^{II}PMA]^+$ solution in CD_3OD/CD_3CD_2OD and $[Fe^{II}PMA]^+$ solid in fluorolube from 5 000 to 30 000 cm^{-1}: (a) solution Abs spectrum at 8 K; (b) solution MCD spectrum at 5 K and 6 T; (c) solid MCD spectrum at 5 K and 6 T.

coordinate, distorted octahedral geometry at the ferrous active site. Ligand field peaks for Fe^{II}BLM are summarized in Table 1. MCD data for a solid sample of Fe^{II}BLM prepared in the absence of any glassing agent also exhibits two bands centered around 11 000 cm^{-1} with a ^5E_g splitting of <3000 cm^{-1} demonstrating that the presence of glassing agent does affect the metal center coordination sphere.

The intensities of the MCD features arising from the transitions $d_{yz} \rightarrow d_{z^2}$ and $d_{yz} \rightarrow d_{x^2-y^2}$ are inversely proportional to temperature which is indicative of *C*-term behavior[68,69] and therefore a degenerate electronic ground state (*i.e.*, $M_s = \pm 2$) with $D < 0$ in the spin Hamiltonian model, which corresponds to the doublet resulting from in-state spin–orbit coupling of the ^5E_g ground state, in the full Hamiltonian description in Figure 2. VTVH MCD saturation magnetization data for Fe^{II}BLM taken at 9433 cm^{-1} are plotted as a function of the reduced parameter $\beta H/2kT$ for a series of fixed temperatures in Figure 5c. VTVH data were collected on both d → d bands and produced nearly identical ground state parameters. These isotherms exhibit nesting behavior (*i.e.*, do not superimpose) resulting from zero-field-splitting of the ground state,[39,40] as has been observed for other $S > {}^1/_2$ metal sites.[70–72] For the $S = 2$ ions, the nesting of these isotherms is due to magnetic field induced splitting and mixing of the wave functions of the lowest, rhombically split, non-Kramers doublet in Figure 2 (right) producing differential amounts of complex character which increase nonlinearly with magnetic field. In addition to the nesting behavior, the curves do not exhibit complete saturation at low temperatures and high fields, but rather continue to increase linearly. Pure non-Kramers doublet behavior will produce isotherms that are saturated at 1.6 K and 7 T, therefore this reflects a contribution from an additional linear field induced mixing mechanism with higher-lying states (*B*-term).[73] The expression for MCD intensity of a rhombically zero-field-split non-Kramers doublet[40] with a linear B-term contribution is given in eq 1:

$$I = A_{\text{sat lim}} \int_0^1 \frac{\cos^2\theta}{\sqrt{\frac{\delta^2}{(g_{\parallel}\beta H)^2} + \cos^2\theta}} \times \tanh\left[\frac{\sqrt{\delta^2 + (g_{\parallel}\beta H \cos\theta)^2}}{2kT}\right] \mathrm{d}\cos\theta + B_0 H \quad (1)$$

where I is the experimental MCD intensity, $A_{\text{sat lim}}$ is an intensity scaling factor, θ is the angle between the external magnetic field

(68) Piepho, S. B.; Schatz, P. N. *Group Theory in Spectroscopy with Applications to Magnetic Circular Dichroism*; John Wiley & Sons, Inc.: New York, 1983.

(69) Schatz, P. N.; McCafferty, A. J. *Q. Rev. Chem. Soc.* **1967**, *23*, 552–584.

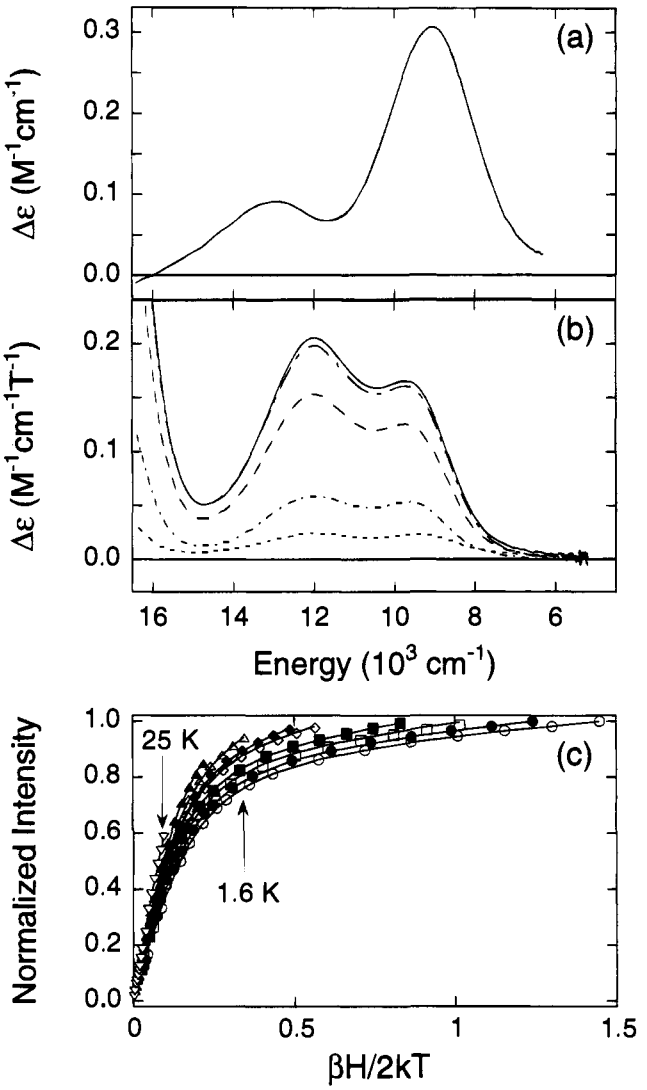

Figure 5. Expanded view of the $Fe^{II}BLM$ (a) CD spectrum at 278 K and (b) MCD spectra at 7 T and 1.6 K (—), 5.0 K (— - —), 15 K (— —), 50 K (— • —), and 150 K (- - -) in the ligand field energy region from 5 000 to 16 000 cm^{-1}. (c) Variable-temperature variable-field saturation magnetization behavior for $Fe^{II}BLM$ recorded at 1060 nm and 1.6 K (○), 1.9 K (●), 2.3 K (□), 2.8 K (■), 4.2 K (◇), 5.0 K (◆), 7.0 K (△), 11.0 K (▲), and 25 K (▽) and magnetic fields ranging from 0 to 7 T. The MCD intensity is normalized and plotted (symbols) as a function of $\beta H/2kT$. The fit to the VTVH MCD data (solid lines) was generated from the parameters given in Table 1. Errors in the MCD intensity are negligible with respect to the symbol size used.

and the molecular zero-field axis, δ is the magnitude of the zero-field-splitting of the non-Kramers doublet ground state (Figure 2, right), H is the applied magnetic field, T is the temperature, β is the Bohr magneton, k is the Boltzmann constant, and B_0 is the linear B-term contribution expressed as a percent of the normalized MCD intensity. Values of $A_{\text{sat lim}}$, $g_{\parallel}$, δ, and B_0 are determined by iteratively fitting eq 1 to the experimental MCD intensities in Figure 5 using a simplex routine. For $Fe^{II}BLM$ the best fit ground state parameters are $g_{\parallel} = 9.3$ and $\delta = 2.4$ cm^{-1} with a significant B-term contribution of 1.5% as summarized in Table 1. Equation 1 assumes that the electronic transition used for the saturation magnetization curves is purely xy-polarized and there is no Zeeman splitting in the x,y-direction (*i.e.*, $g_{\perp} = 0$). Allowing for the effects of z-polarization in the $Fe^{II}BLM$ (and $[Fe^{II}PMA]^+$ in solution, *vide infra*) analysis returns the same values for the ground state parameters, while application of a three-level $+D$ model[74] results in unphysical parameters.

Table 1. $Fe^{II}BLM$ and $[Fe^{II}PMA]^+$ Ligand Field Transition Energies, Excited State Splittings, and Ground State Spin Hamiltonian Parameters

		$Fe^{II}BLM$		$[Fe^{II}PMA]^+$	
		solution		solution	solid
band		RT CD	LT MCD	MCD	MCD
1	energy (cm^{-1})	9100	9400	10090	5100[a]
	fwhm (cm^{-1})	2820	3940	2340	2700[b]
2	energy (cm^{-1})	13050	12050	12200	11200
	fwhm (cm^{-1})	2700	2420	2800	4000
	Δ^5E_g (cm^{-1})	3950	2650	2110	6100
	$A_{\text{sat lim}}$		1.8	2.0	1.4
	B_0 (%)		1.5	0.2	4.7
	$g_{\parallel}$		9.3	9.0[c]	8.5
	δ (cm^{-1})		2.4	2.4[c]	3.3
	$-\Delta$ (cm^{-1})		800	950	900
	V (cm^{-1})		280	450	600

[a] Estimate obtained from peak maximum in Figure 7. [b] Estimate obtained from full width at half maximum height in Figure 7. [c] Due to noise in the data, a range of values is obtained depending on which temperature set is employed in the calculation ($8.6 < g < 9.4$, $2.2 < \delta < 2.6$ cm^{-1}). The average values have been used to obtain Δ and V.

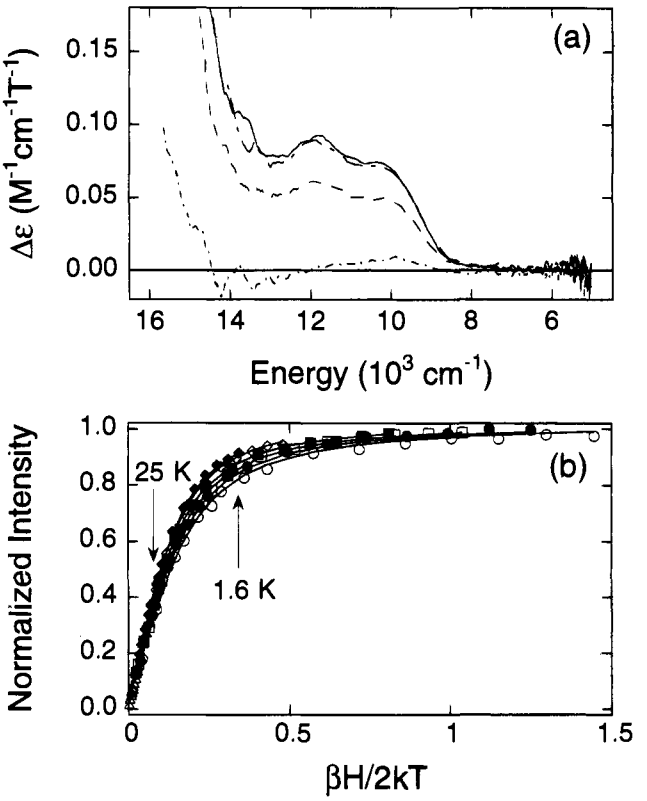

Figure 6. (a) Ligand field region MCD spectra of $[Fe^{II}PMA]^+$ in 1:4 CD_3OD:CD_3CD_2OD. MCD spectra were obtained at 7 T and 1.6 K (—), 5.0 K (— - —), 15 K (— —), and 50 K (— • —). (b) Variable-xtemperature variable-field MCD of $[Fe^{II}PMA]^+$ in solution recorded at 1000 nm and 1.6 K (○), 1.9 K (●), 2.3 (□), 2.8 K (■), 5.0 K (◇), 7.0 K (◆), and 25 K (△) and magnetic fields ranging from 0 to 7 T. Traces obtained at 4.2 and 11 K have been omitted for clarity. The MCD intensity is normalized and plotted (symbols) as a function of $\beta H/2kT$. The fit to these data (solid lines) was derived from the parameters given in Table 1. Errors in the MCD intensities are smaller than the symbol size used.

(70) Johnson, M. K.; Robinson, A. E.; Thomson, A. J. In *Iron Sulfur Proteins*; Spiro, T. G., Ed.; Wiley: New York, 1979; Vol. 4, pp 367–406.
(71) Thomson, A. J.; Johnson, M. K. *Biochem. J.* **1980**, *191*, 411–420.
(72) Werth, M. T.; Johnson, M. K. *Biochemistry* **1989**, *28*, 3982–3988.
(73) Mabrouk, P. A.; Orville, A. M.; Lipscomb, J. D.; Solomon, E. I. *J. Am. Chem. Soc.* **1991**, *113*, 4053–4061.

$[Fe^{II}PMA]^+$ isolated as a racemic mixture is not optically active and therefore exhibits no CD intensity. However, two ligand field transitions are observed in the MCD spectrum of $[Fe^{II}PMA]^+$ in solution (Figure 4b, expanded in Figure 6a). Similar to $Fe^{II}BLM$, the temperature dependence of these bands demonstrates *C*-term behavior and indicates the same sign of the zero-field-splitting parameter ($D < 0$). These transitions can be Gaussian resolved into two features at 10 090 and 12 200 cm^{-1} with $\Delta^5E_g \approx 2110$ cm^{-1}, indicating a six-coordinate site structure for $[Fe^{II}PMA]^+$ in solution. These transitions are slightly higher in energy and possess a smaller Δ^5E_g splitting than those of $Fe^{II}BLM$, implying less distortion (*i.e.*, no weak axial ligand) at the ferrous center. VTVH MCD saturation magnetization data were obtained at 9 900 (shown in Figure 6b) and 11 900 cm^{-1}; the energies are lower than the true transition maxima in order to avoid a significant contribution from the tail of the CT transition at higher energy. Fitting of the saturation data with eq 1 yields the ground state parameters $g_{||} = 9.0$ and $\delta = 2.4$ cm^{-1} as well as a small *B*-term contribution of 0.2%, which is consistent with the fact that the MCD intensity saturates in Figure 6b.

MCD spectra were also collected for solid samples of $[Fe^{II}PMA]^+$ with both Cl^- and I^- counterions. No appreciable difference between the spectra of the two solid species is observed. The low-energy region in Figure 4c is expanded in Figure 7a. Three transitions are observed: a CT band highest in energy and two ligand field bands exhibiting *C*-term behavior which are visible at 5 100 and 11 200 cm^{-1} with an excited state splitting, Δ^5E_g, of 6100 cm^{-1}. As the low-energy band extends beyond the low-energy limits of our detection, its energy and full width at half maximum (fwhm) height in Table 1 are estimated from a Gaussian fit. From Figure 2, an excited state energy splitting, Δ^5E_g, greater than 5000 cm^{-1} and the presence of a low-energy transition are indicative of a five-coordinate structure, with the position of the highest energy spin-allowed transition above 10 000 cm^{-1} suggesting that the geometry at the Fe^{2+} center is closer to square pyramidal than trigonal bipyramidal.[66,75-78] VTVH MCD saturation magnetization data obtained at 5100 cm^{-1} are shown in Figure 7b. Fitting eq 1 to the experimental data gives $g_{||} = 8.5$, $\delta = 3.3$ cm^{-1}, and a large *B*-term contribution of 4.7% which is evident from the lack of saturating behavior at low temperature and high field in Figure 7b. The value of $g_{||}$ increases slightly (to 8.9) when *z*-polarization is included and a three-level $+D$ fit gives results consistent with the $D < 0$ analysis as both are in the rhombic limit.

The value obtained for δ of 3.3 cm^{-1} for solid $[Fe^{II}PMA]^+$ is consistent with other five-coordinate species whereas the value of 2.4 cm^{-1} for both $[Fe^{II}PMA]^+$ and $Fe^{II}BLM$ in solution is unusually small for six-coordinate complexes of similar ligation.[40] Correspondingly, the $^5T_{2g}$ splittings (Δ and *V*) in Figure 2 obtained from these spin Hamiltonian parameters show large deviations from the expected values. Typical five-coordinate parameters are observed for solid $[Fe^{II}PMA]^+$ with $-\Delta \approx 900$ cm^{-1} and $V \approx 600$ cm^{-1} ($V/2\Delta \approx 0.33$). However, for $[Fe^{II}PMA]^+$ in solution, $-\Delta$ increases slightly to ~950 cm^{-1} with $V \approx 450$ cm^{-1} which is in contrast to the expected decrease in the t_{2g} (and e_g) orbital splittings based on the closer to octahedral geometry in the six-coordinate site. A decrease in the ^5E_g excited state splitting is in fact observed. Similarly for $Fe^{II}BLM$, a large $-\Delta \approx 800$ cm^{-1} is also obtained with $V \approx 280$ cm^{-1}. These large $^5T_{2g}$ ground state splittings for $Fe^{II}BLM$ and $[Fe^{II}PMA]^+$ in solution indicate the presence of significant d_π orbital interactions which deviate from other non-heme Fe^{2+} sites, suggesting an unusually strong ligand–metal π-bond for these six-coordinate complexes.

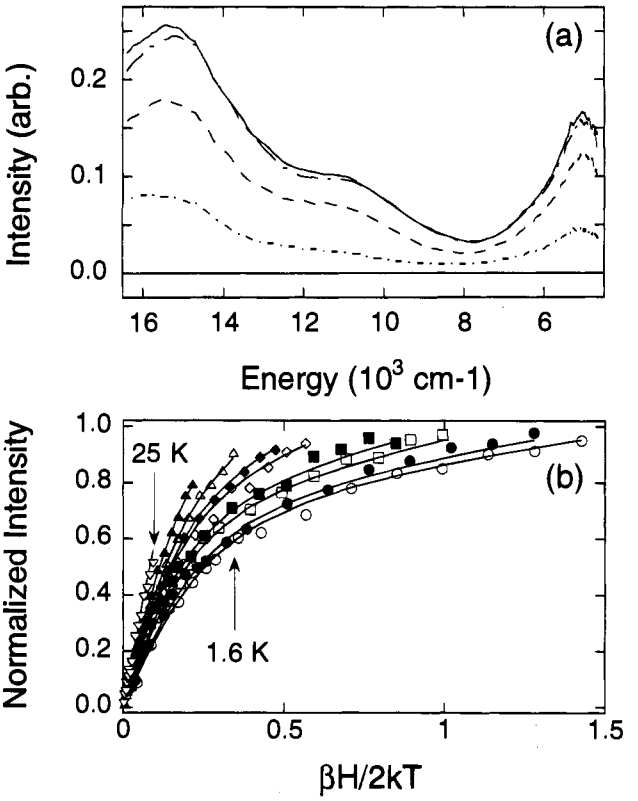

Figure 7. (a) Temperature dependence of the ligand field energy region MCD spectra of solid $[Fe^{II}PMA]^+$ recorded at 7 T and 1.6 K (—), 5.0 K (— - —), 15 K (— —), and 50 K (— • —). (b) Saturation magnetization behavior for $[Fe^{II}PMA]^+$ solid recorded at 1930 nm and 1.6 K (○), 1.9 K (●), 2.3 K (□), 2.8 K (■), 4.2 K (◇), 5.0 K (◆), 7.0 K (△), 11.0 K (▲), and 25 K (▽) and magnetic fields ranging from 0 to 7 T. The normalized MCD intensity is plotted (symbols) as a function of $\beta H/2kT$ and fit (solid lines) with the parameters given in Table 1. Error in the MCD intensity is less than the symbol size.

Table 2. $Fe^{II}BLM$ and $[Fe^{II}PMA]^+$ Abs, CD, and MCD Gaussian Fitting Results in the Charge Transfer Energy Region

	energy (full width at half maximum height)[a] in cm^{-1}		
	$Fe^{II}BLM$	$[Fe^{II}PMA]^+$	
band	solution	solution	solid
1	18 100 (3700)	13 120 (1580)	
2	20 350 (3800)	14 430 (1810)	
3	22 690 (3700)	15 650 (3000)	14 565 (3390)
4	26 040 (4500)	17 960 (4800)	16 410 (3670)
5	29 000 (4600)	20 265 (4300)	18 350 (3900)

[a] Energy and full width at half maximum height are accurate within ± 100 cm^{-1}.

2. Charge Transfer Region. From Figures 3 and 4 a number of moderately-intense low-energy CT bands are observed in addition to the ligand field transitions exhibited by both $Fe^{II}BLM$ and $[Fe^{II}PMA]^+$. The energies and fwhm's resulting from the Gaussian analysis of these observed spectral features are summarized in Table 2. The Abs, CD, and MCD spectra of $Fe^{II}BLM$ in the CT region are Gaussian resolved in Figure 8. Abs, CD, and MCD spectra exhibit features arising

(74) Campochiaro, C.; Pavel, E. G.; Solomon, E. I. Submitted for publication.
(75) Riley, D. P.; Merrell, P. H.; Stone, J. A.; Busch, D. H. *Inorg. Chem.* **1975**, *14*, 490–494.
(76) Chia, P. S. K.; Livingstone, S. E. *Aust. J. Chem.* **1969**, *22*, 1613–1625.
(77) Ciampolini, M.; Nardi, N. *Inorg. Chem.* **1966**, *5*, 1150–1154.
(78) Stoppioni, P.; Mani, F.; Sacconi, L. *Inorg. Chim. Acta* **1974**, *11*, 227–230.

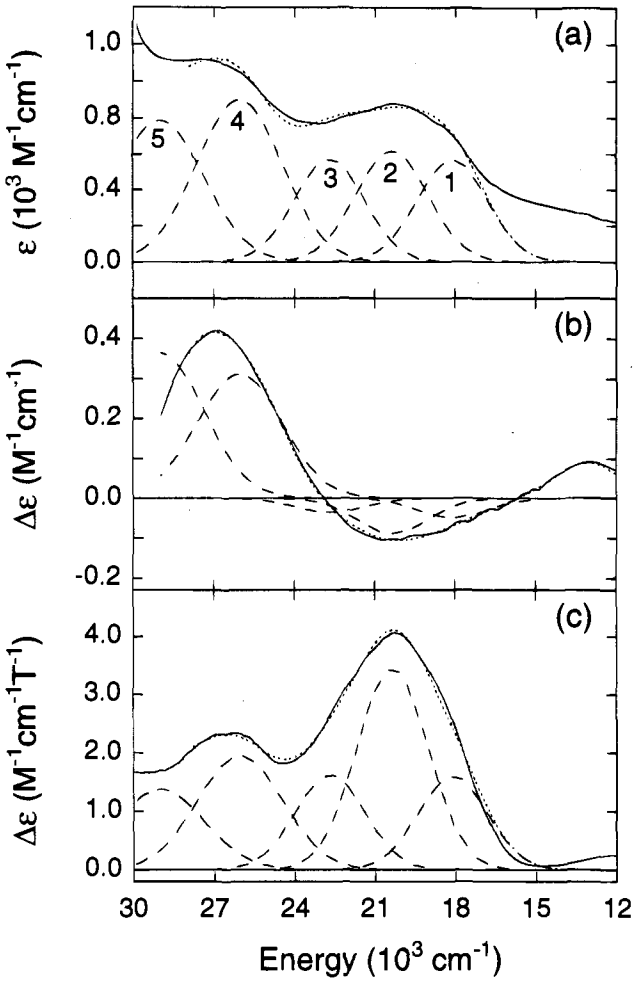

Figure 8. Gaussian resolution of the $Fe^{II}BLM$ charge transfer transitions observed in the Abs, CD, and MCD spectra: (a) Abs spectrum at 8 K; (b) CD spectrum at 278 K; (c) MCD spectrum at 5 K and 6 T. The experimental spectra (—) were simultaneously fit to individual Gaussian bandshapes (— —) and plotted against the resultant sum (•••). The individual Gaussians are numbered 1 to 5 in order of increasing energy as listed in Table 2.

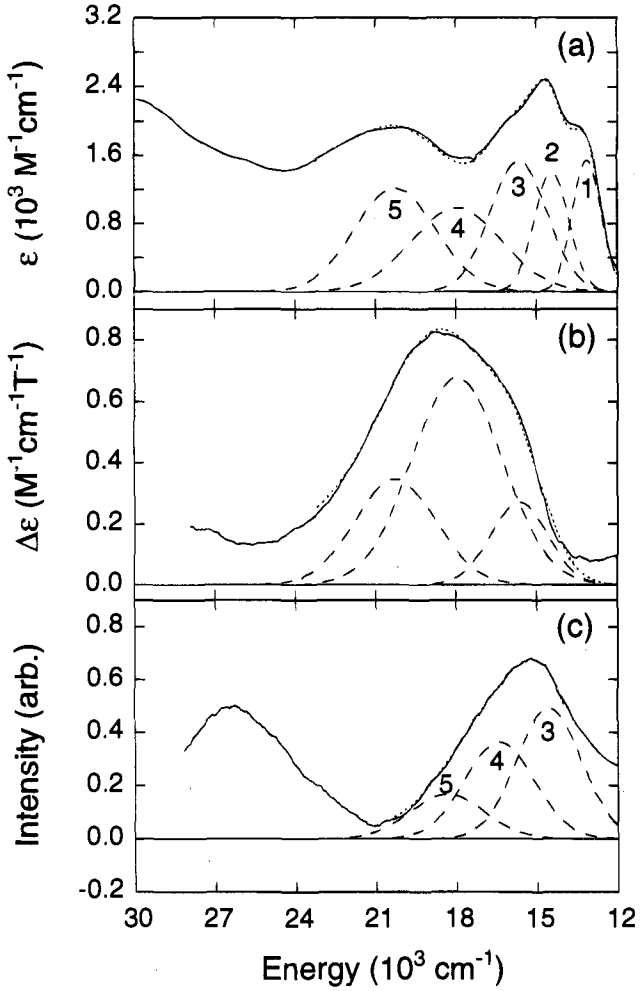

Figure 9. Gaussian resolution of $[Fe^{II}PMA]^+$ solid and solution charge transfer transitions observed in the Abs and MCD spectra: (a) Abs spectrum of the solution at 8 K; (b) MCD spectrum of the solution at 5 K and 6 T; (c) MCD spectrum of the solid at 5 K and 6 T. The experimental spectra (—) were simultaneously fit to individual Gaussian bandshapes (— —) and plotted against the resultant sum (•••). The individual Gaussians are numbered 1 to 5 in order of increasing energy as listed in Table 2. Bands 1 and 2 in the Abs spectrum are not observed in either MCD spectrum as discussed in the text.

from the same set of transitions (same energy position and fwhm at the same temperatures), varying only in the sign and magnitude of the individual contributions due to differences in selection rules for the different spectroscopic methods. Three bands are required to accurately fit the area under the lowest energy envelope of the Abs and MCD spectra (Figure 8, spectra a and c) and two are necessary in the second energy region. Iterative fitting of these five bands to the Abs and MCD spectra places Band 1 at ~18 000 cm^{-1}, Band 2 at ~20 350 cm^{-1}, Band 3 at ~22 690 cm^{-1}, Band 4 at ~26 040 cm^{-1}, and Band 5 at ~29 000 cm^{-1} (Table 2). Due to the difficulty in accounting for baseline effects at the extrema of the low-temperature Abs spectrum, a greater error exists in the energies and fwhm's of Bands 1 and 5 derived from simultaneously fitting the Abs and MCD spectra. The RT CD spectrum can also be fit with the same Gaussian band energies and fwhm's to those obtained from the Abs and MCD fitting analysis.

The transitions in the low-temperature Abs and MCD spectra of $[Fe^{II}PMA]^+$ in solution (Figure 9, spectra a and b) do not correlate with one another as clearly as those of $Fe^{II}BLM$ (Figure 8, spectra a and c). Results of simultaneous fitting of the five lowest energy transitions position Band 1 at ~13 120 cm^{-1}, Band 2 at ~14 430 cm^{-1}, Band 3 at ~15 650 cm^{-1}, Band 4 at ~17 960 cm^{-1}, and Band 5 at ~20 265 cm^{-1} (Table 2). The two lowest energy transitions (1 and 2) observed in the Abs spectra have little MCD intensity. The remaining intensity of positive sign at 13 000 cm^{-1} in the MCD spectrum is due in part to contributions from the ligand field transitions (see Figure 4b) at slightly lower energy. Although the Abs spectrum of solid $[Fe^{II}PMA]^+$ is not shown due to the effects of scattering on the baseline, similar features to $[Fe^{II}PMA]^+$ in solution are observed, but they are shifted to lower energy. The lowest energy envelope of the low-temperature MCD spectrum of solid $[Fe^{II}PMA]^+$ (Figure 9c) is also red shifted and can be individually fit to three intense bands at ~14 565, ~16 410, and ~18 350 cm^{-1} with the tail to lower energy having possible contributions from the CT bands observed in the mull Abs spectrum as wellas the ligand field transition at 11 200 cm^{-1} in the mull MCD spectrum (see Figure 4c). Based on the shift to lower energy of these CT transitions demonstrated by the Abs spectrum, and the similarity of their fwhm's to Bands 3, 4, and 5 in the solution $[Fe^{II}PMA]^+$ MCD spectrum, these MCD features of solid $[Fe^{II}PMA]^+$ are assigned as having the same origin (Table 2).

The low-energy CT transitions of $[Fe^{II}PMA]^+$ (and $Fe^{II}BLM$) can be assigned by comparison to the Abs spectra of the structurally perturbed analogs $[Fe^{II}(Prpep)_2]$, $[Fe^{II}(Pypep)_2]$, and $[Fe^{II}PMD]^+$. The Abs spectra in the CT region (Figure 10) of $[Fe^{II}PMA]^+$ and $[Fe^{II}PMD]^+$ have the same low-energy bands,

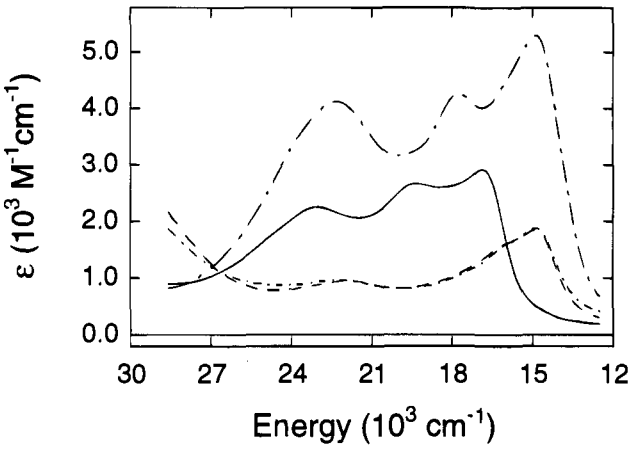

Figure 10. Room temperature absorption spectra of $[Fe^{II}(Pypep)_2]$ (—), $[Fe^{II}(Prpep)_2]$ (— - —), $[Fe^{II}PMA]^+$ (— —), and $[Fe^{II}PMD]^+$ (— • —) in MeOH. Note that the spectra of $[Fe^{II}PMA]^+$ and $[Fe^{II}PMD]^+$ are virtically superimposable.

arguing against histidine contributions to the CT transitions, while the bands in $[Fe^{II}(Pypep)_2]$ are shifted by 0.20 eV to higher energy relative to $[Fe^{II}(Prpep)_2]$ consistent with the increase in the redox potential of 0.21 eV.[55] These comparisons demonstrate that the low-energy region of $[Fe^{II}PMA]^+$ is composed of iron(II) → pyrimidine CT transitions, as is further supported by the rR studies below, which can be correlated with the CT transitions in the Abs, CD, and MCD spectra of $Fe^{II}BLM$. The following trend in the iron(II) → pyrimidine CT energies results from these assignments: $Fe^{II}BLM$ > $[Fe^{II}PMA]^+$ in solution > $[Fe^{II}PMA]^+$ solid; the intensity trend is the reverse. These trends indicate increasing Fe^{2+}—pyrimidine π-backbonding along the series that is influenced by pyrimidine ring substituents and change in coordination number (see Discussion).

B. Resonance Raman. The rR spectrum of $[Fe^{II}PMA]^+$ was assigned based on deuterium isotope effects and comparison to $[Fe^{II}(Prpep)_2]$, $[Fe^{II}(Pypep)_2]$, and $[Fe^{II}PMD]^+$ as well as correlation to representative spectra for substituted pyrimidines and pyridines in solution,[79-86] and is discussed in order of increasing vibrational frequency. Profiles of the vibrations over the CT region are then used to confirm the assignment of the bands in the low-energy envelope of the Abs spectrum of $[Fe^{II}PMA]^+$ (and $Fe^{II}BLM$) as iron(II) → pyrimidine CT transitions. Excitation at 647 nm for $[Fe^{II}PMA]^+$, $[Fe^{II}(Prpep)_2]$, and $[Fe^{II}(Pypep)_2]$ produces the spectra shown in Figure 11. The rR spectrum of $[Fe^{II}PMD]^+$ is extremely similar to that of $[Fe^{II}PMA]^+$ and is not shown. $[Fe^{II}PMA]^+$ and $[Fe^{II}PMD]^+$ show deuterium exchange with solvent while $[Fe^{II}(Prpep)_2]$ and $[Fe^{II}(Pypep)_2]$ are insensitive to substitution. The bands in $[Fe^{II}PMA]^+$ have depolarization ratios of ~1/3, indicating that all observed vibrations are of A_1 symmetry.

The rR spectrum of $[Fe^{II}PMA]^+$ between 600 and 900 cm^{-1} has four moderately strong vibrations at 680, 706, 744, and 848 cm^{-1}. All four peaks exhibit large isotope shifts to lower frequency of 12, 18, 12, and 11 cm^{-1} in methanol-d_4, respectively. Peaks in this region are observed in the rR spectra of $[Fe^{II}(Prpep)_2]$ at 688 and 710 cm^{-1} and $[Fe^{II}(Pypep)_2]$ at 650 cm^{-1}. These features can be assigned to in- and out-of-plane ring deformations which are shifted due to the substitution of pyridine for pyrimidine in $[Fe^{II}(Pypep)_2]$. Additionally, for $[Fe^{II}(Pypep)_2]$ a vibration at 695 cm^{-1} and a weak band at 855 cm^{-1} are observed which are assigned as out-of-plane C—H deformations of the pyridine ring and suggest the parallel assignment for the 744 and 848 cm^{-1} vibrations in the $[Fe^{II}PMA]^+$ spectrum, consistent with their large deuterium isotope shifts. Although ring vibrations do exist in this energy region and cannot be ruled out as possible assignments, the small deuterium shifts observed for higher frequency ring stretches (*vide infra*) do not support this possibility.

Between 900 and 1100 cm^{-1} the spectra of pyridines and pyrimidines in solution are dominated by ring stretching and breathing modes but metal chelation and ring substitution drastically decrease their intensities. Observation of these modes in methanol is further complicated by the broad solvent peak at 1034 cm^{-1} which partially obscures these features. This is evident in the rR spectrum of $[Fe^{II}PMA]^+$ where these bands show minimal intensity even though they are discernible in the rR spectra of $[Fe^{II}(Prpep)_2]$ at 988 and 1013 cm^{-1} and $[Fe^{II}(Pypep)_2]$ at 988 and 1028 cm^{-1}.

At higher frequency, 1100—1500 cm^{-1}, the spectra of $[Fe^{II}PMA]^+$, $[Fe^{II}(Prpep)_2]$, and $[Fe^{II}(Pypep)_2]$ increase in complexity. Although no vibration is observed in the rR spectrum of $[Fe^{II}PMA]^+$ near ~1150 cm^{-1}, moderately-intense bands are observed in the spectra of $[Fe^{II}(Pypep)_2]$ and $[Fe^{II}(Prpep)_2]$ at 1151 and 1156 cm^{-1}, respectively, which can be assigned as in-plane C—H deformations. A weak ring mode appears in the rR spectrum of $[Fe^{II}PMA]^+$ at 1198 cm^{-1} which has negligible intensity for $[Fe^{II}(Prpep)_2]$ but is somewhat more intense in the rR spectrum of $[Fe^{II}(Pypep)_2]$ at 1195 cm^{-1}. $[Fe^{II}PMA]^+$ also exhibits a vibration with moderate intensity at 1232 cm^{-1} which is observed in the spectra of $[Fe^{II}(Prpep)_2]$ and $[Fe^{II}(Pypep)_2]$ at 1236 cm^{-1} with weak shoulders to lower energy. These bands are assigned as in-plane C—H deformations based on the frequency of the vibrations; however, the band for $[Fe^{II}PMA]^+$ exhibits no deuterium shift, suggesting the possibility of an alternate ring mode assignment. The vibrations at 1290 and 1285 cm^{-1} in the spectra of $[Fe^{II}PMA]^+$ and $[Fe^{II}(Prpep)_2]$, respectively, are also assigned to pyrimidine ring modes which have been observed at similar frequencies in the Raman spectra of substituted pyrimidines and correspond to the 1256 cm^{-1} pyridine ring mode in the $[Fe^{II}(Pypep)_2]$ spectrum. For $[Fe^{II}PMA]^+$ this vibration exhibits a 2-cm^{-1} shift upon deuterium exchange, indicating that these normal modes do not directly involve participation by exchangeable protons. Several vibrations contribute to a multiplet centered at 1359 cm^{-1} in the rR spectrum of $[Fe^{II}PMA]^+$. This maximum corresponds to the vibrations at 1345 and 1347 cm^{-1} in the rR spectra of $[Fe^{II}(Prpep)_2]$ and $[Fe^{II}(Pypep)_2]$ which are assigned as pyrimidine and pyridine ring modes, respectively. On the high-energy side of the multiplet, the vibration at 1379 cm^{-1} in the $[Fe^{II}PMA]^+$ spectrum correlates with the pyrimidine and pyridine ring stretches at 1389 and 1382 cm^{-1} in the rR spectra of $[Fe^{II}(Prpep)_2]$ and $[Fe^{II}(Pypep)_2]$, respectively. In fully deuterated solvent, the components of the multiplet in the $[Fe^{II}PMA]^+$ spectrum exhibit a complex shifting pattern which is difficult to decipher with the exception of a distinct vibration appearing at 1356 cm^{-1}, suggesting the possible coupling of pyrimidine ring modes to vibrations involved in hydrogen bonding. The

(79) Green, J. H. S.; Kynaston, W.; Paisley, H. M. *Spectrochim. Acta* **1963**, *19*, 549—564.
(80) Lafaix, A. J.; Lebas, J. M. *Spectrochim. Acta* **1970**, *26A*, 1243—1270.
(81) Lord, R. C.; Marston, A. L.; Miller, F. A. *Spectrochim. Acta* **1957**, *9*, 113—125.
(82) Milani-Nejad, F.; Stidham, H. D. *Spectrochim. Acta* **1975**, *31A*, 1433—1453.
(83) Sbrana, G.; Adembri, G.; Califano, S. *Spectrochim. Acta* **1966**, *22*, 1831—1842.
(84) Takahashi, S.; Sam, J. W.; Peisach, J.; Rousseau, D. L. *J. Am. Chem. Soc.* **1994**, *116*, 4408—4413.
(85) Wright, P. G.; Stein, P.; Burke, J. M.; Spiro, T. G. *J. Am. Chem. Soc.* **1979**, *101*, 3531—3535.
(86) Zarembowitch, J. *J. Chim. Phys.* **1976**, *73*, 407—412.

rR spectrum of $[Fe^{II}PMA]^+$ also displays two strong vibrations at 1425 and 1443 cm^{-1} which are assigned as ring stretches based on the observation of similar features in the Raman spectra of substituted pyrimidines and the appearance of parallel vibrations at 1458 and 1464 cm^{-1} in the rR spectrum of $[Fe^{II}(Prpep)_2]$ and a single band at 1465 cm^{-1} in that of $[Fe^{II}(Pypep)_2]$. Upon deuteration, the $[Fe^{II}PMA]^+$ vibrations at 1425 and 1443 cm^{-1} coalesce to a single feature at 1436 cm^{-1} possessing approximately twice the integrated intensity, also suggesting the presence of proton motion in these normal modes.

The most intense features of the $[Fe^{II}PMA]^+$ rR spectrum are vibrations at 1519 and 1542 cm^{-1} which correspond to the bands at 1533 and 1555 cm^{-1} in the spectra of $[Fe^{II}(Prpep)_2]$ and $[Fe^{II}(Pypep)_2]$, respectively, and are assigned as pyrimidine and pyridine ring stretches in accordance with their small isotope shifts. These bands are generally observed at 1570 and 1583 cm^{-1} for uncomplexed pyrimidine and pyridine but are shifted to lower energy upon chelation and substitution on the pyrimidine ring in the $[Fe^{II}PMA]^+$ complex. A very weak feature appears at 1587 cm^{-1} for $[Fe^{II}PMA]^+$ and broad, overlapping bands are observed in the rR spectra of $[Fe^{II}(Prpep)_2]$ and $[Fe^{II}(Pypep)_2]$ centered at 1590 and 1608 cm^{-1}, respectively. Similar vibrations have been observed at 1587 cm^{-1} in the IR spectrum of $[Fe^{II}PMA]^+$ [43] and at 1595 cm^{-1} in the rR spectrum of $Fe^{II}BLM$ and have been assigned as an amide I C=O stretch.[84] The diminished intensity of this normal mode in the rR spectrum of $[Fe^{II}PMA]^+$ relative to $[Fe^{II}(Prpep)_2]$ results from the presence of the electron withdrawing Br atom on the pyrimidine ring, which decreases the available electron density that can be delocalized to the amide.[55,84] The coordinated amide C=O stretching mode is less intense in the rR spectrum of $[Fe^{II}(Pypep)_2]$ presumably due to a decrease in the electron-donating ability of the pyridine ring relative to pyrimidine, consistent with the greater redox potential of pyridine. Since $[Fe^{II}PMA]^+$ forms an activated complex with similar DNA cleaving specificity to activated BLM and exhibits poor delocalization of electron density to the coordinated amide, the mechanistic importance of this extended conjugation requires further study.

With the exception of the coordinated amide C=O band, the peaks in the rR spectra of $[Fe^{II}PMA]^+$, $[Fe^{II}(Prpep)_2]$, and $[Fe^{II}(Pypep)_2]$ in Figure 11 almost exclusively result from normal modes of the aromatic nitrogen heterocycle with the specific assignments summarized in Table 3. The vibrational assignments confirm that the low-energy Abs bands of these complexes (Figure 10), which show resonance with 647-nm excitation, contain CT character involving the pyrimidine or pyridine ligands with no contribution from the imidazole ligand. In order to profile the low-energy CT bands in the room temperature Abs spectrum of $[Fe^{II}PMA]^+$, a series of rR spectra of this complex were obtained using laser excitation between 560 and 752 nm. The rR spectra show strong enhancement across this region as evident in the representative spectra shown at 676, 647, and 568 nm in Figure 12a. The pronounced decrease in resonance enhancement from 676 to 568 nm excitation is due to the decline in Abs intensity toward a minimum in the room temperature Abs spectrum in Figure 10. There is differential intensity enhancement of some peaks over the 560−752-nm region; for example, at 676 nm the 1519-cm^{-1} vibration is more intense than the 1542-cm^{-1} vibration while at 568 nm the inverse relationship is observed. Profiles of four prominently resonance enhanced vibrations at 680, 744, 1519, and 1542 cm^{-1}, which are assigned as in-plane ring and out-of-plane C−H deformations, and pyrimidine ring stretches (Table 3) are shown in Figure 12b. Three peaks are observed in the rR profiles over the $[Fe^{II}PMA]^+$ Abs spectrum, demonstrating the presence of three CT bands beneath the low-energy envelope in the 560−750-nm region with maxima at 600, 650, and 680 nm. This analysis is consistent with the Gaussian resolved energies of Bands 1−3 in the low-temperature $[Fe^{II}PMA]^+$ solution Abs and MCD spectra in Figure 9 (spectra a and b) with a shift of ~800 cm^{-1} due to the temperature difference. The fact that the pyrimidine ring modes show strong enhancement over all three Abs bands indicates that these can be assigned as iron(II) → pyrimidine CT transitions.

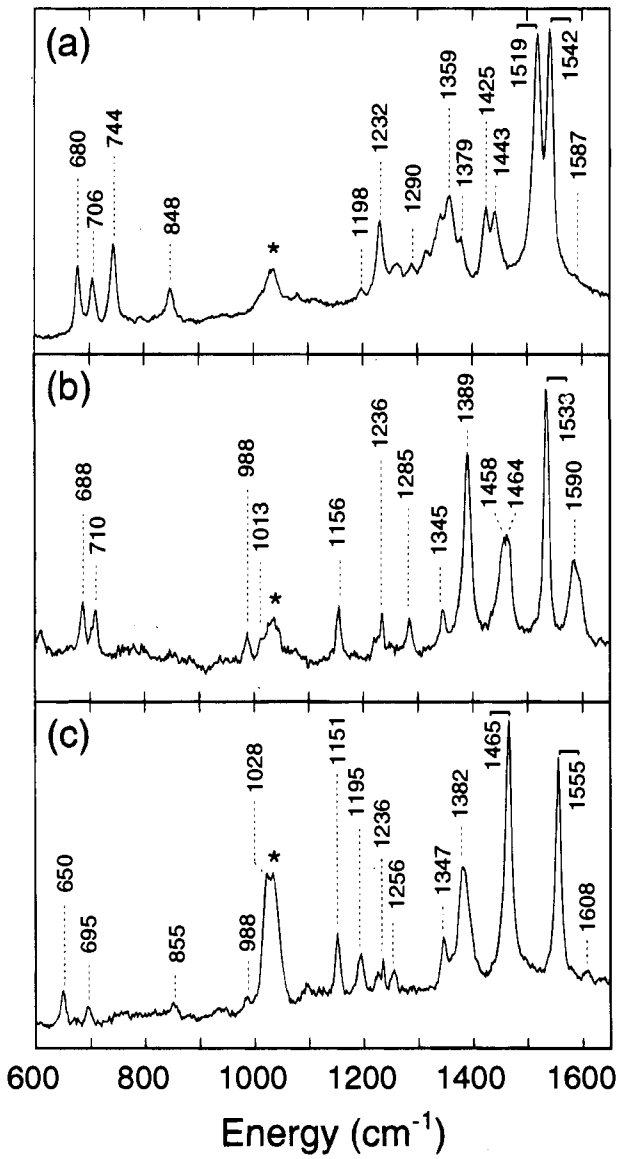

Figure 11. Room temperature resonance Raman spectra of (a) $[Fe^{II}PMA]^+$, (b) $[Fe^{II}(Prpep)_2]$, and (c) $[Fe^{II}(Pypep)_2]$ in MeOH obtained with 647-nm excitation. Vibrational frequencies (in cm^{-1}) correspond to the assignments in Table 3. Solvent peaks are denoted with asterisks (*).

C. X-ray Absorption Spectroscopy. Fe K-edge X-ray absorption spectra of $[Fe^{II}PMA]^+$ solid, $[Fe^{II}PMA]^+$ solution, and $Fe^{II}BLM$ are shown in Figure 13a. The lowest energy peaks arise from the weak 1s → 3d pre-edge transition which is at ~7112 eV followed by the 1s → 4p transition at ~7127 eV. An expanded view of the 1s → 3d pre-edge region is shown for the same samples in Figure 13b. Figure 13c contains the 1s → 3d pre-edge region of representative five- and six-coordinate high-spin ferrous model complexes, $[Fe(TMC)N_3]BF_4$[66] and $[Fe(imidazole)_6]Cl_2$,[67] respectively. The $[Fe(imidazole)_6]Cl_2$ spectrum (solid line) has two very weak pre-edge features at ~7111.5 and ~7113.5 eV, while the [Fe-

Table 3. Resonance Raman Vibrational Frequencies (cm^{-1}) of $[Fe^{II}PMA]^+$, $[Fe^{II}(Prpep)_2]$, and $[Fe^{II}(Pypep)_2]$ in MeOH Obtained with 647-nm Excitation

$[Fe^{II}$-PMA$]^+$	Δ^a	$[Fe^{II}$-(Prpep)$_2]$	$[Fe^{II}$-(Pypep)$_2]$	proposed assignment[b]
680	−12	688	650	in-plane ring deformation
706	−18	710		out-of-plane ring deformation
744	−12		695	out-of-plane C−H deformation
848	−11		855	out-of-plane C−H deformation
		988	988	ring stretch
		1013	1028	trigonal ring breathing mode
		1156	1151	in-plane C−H deformation
1198			1195	ring mode
1232		1236	1236	in-plane C−H deformation
1290	−2	1285	1256	ring mode
1359	−3	1345	1347	ring mode
1379	*c*	1389	1382	ring stretch
1425	+10	1458		ring stretch
1443	−8	1464	1465	ring stretch
1519	−2			ring stretch
1542	−3	1533	1555	ring stretch
1587		1590	1608	amide I C=O stretch

[a] Deuterium isotope shifts for $[Fe^{II}PMA]^+$ (Δ) are given in cm^{-1}. [b] Assignments made using refs 79–83, 85, and 86. [c] Deuterium isotope shift could not be accurately determined as discussed in the text.

$(TMC)N_3]BF_4$ spectrum (dashed line) has a much more intense feature at 7111.5 eV (Figure 13c). The spectra of $[Fe^{II}PMA]^+$ solid (solid line) and $[Fe^{II}PMA]^+$ solution (dashed line) show two features at ~7112 and ~7113.5 eV with the first transition at 7112 eV for $[Fe^{II}PMA]^+$ solid being more intense (Figure 13b). The spectrum of $Fe^{II}BLM$ (dotted line) has two weak features at approximately 7111.5 and 7113.5 eV (Figure 13b). The feature at ~7127 eV, attributed to the 1s → 4p transition, is more intense and at slightly lower energy for $Fe^{II}BLM$ relative to that of $[Fe^{II}PMA]^+$ samples. The $[Fe^{II}PMA]^+$ solid feature lies ~1 eV above that of the $[Fe^{II}PMA]^+$ in solution (Figure 13a).

The energy of the 1s → 4p transition is dependent upon the effective nuclear charge of the absorbing metal atom. This charge is governed by a combination of effects including the formal oxidation state of the metal, the number and type of ligating atoms, and the coordination geometry.[87-90] Differences in the edge energy position of the ferrous BLM and PMA complexes in Figure 13a thus reflect variation in the coordination number and the ligand−iron bonding interactions. One would expect the edge of a five-coordinate complex to be at lower energy than that of a six-coordinate complex[90] due to reduced ligand repulsion; however, the edge of $[Fe^{II}PMA]^+$ solid occurs at slightly higher energy than $[Fe^{II}PMA]^+$ solution indicating increased charge donation to the ligand set. This likely reflects the pyrimidine backbonding, which from the edge energy positions follows the trend: $[Fe^{II}PMA]^+$ solid > $[Fe^{II}PMA]^+$ solution > $Fe^{II}BLM$.

The 1s → 3d pre-edge feature can be used to probe the coordination number of an iron active site. The 1s → 3d transition is formally electric dipole forbidden, but gains intensity through an allowed quadrupole transition and more dominantly by 4p mixing into the 3d states as a result of the non-centrosymmetric environment of the metal site. It has been shown for ferric complexes that when the symmetry of the iron

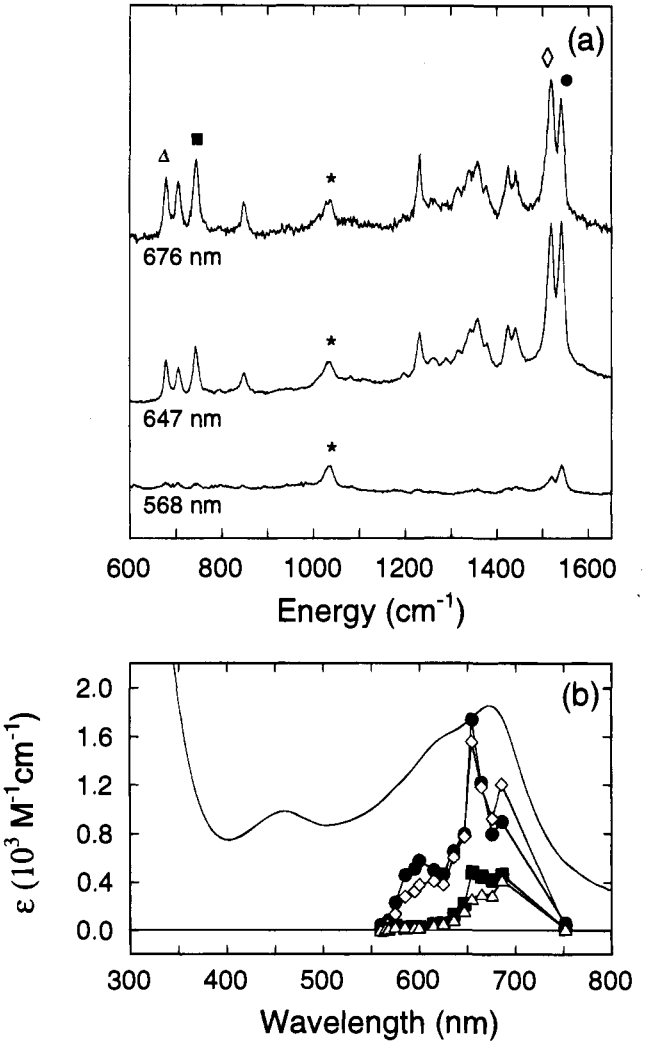

Figure 12. (a) Resonance Raman spectra of $[Fe^{II}PMA]^+$ in MeOH obtained with 676-, 647-, and 568-nm excitation. Solvent peaks are denoted with asterisks (*). All spectra were normalized to the 1034-cm^{-1} band of MeOH. (b) Resonance Raman profiles of the 680- (△), 744- (■), 1519- (◇), and 1542- (●) cm^{-1} vibrations labeled in part a, overlayed with the room temperature absorption spectrum of $[Fe^{II}PMA]^+$ in MeOH.

site is lowered, the pre-edge intensity increases due to an increase in the 3d−4p mixing.[89] In the high-spin ferrous case, two final states of maximum spin multiplicity can be reached, ^4F and ^4P. The free ion splitting of these is 2 eV,[87] and it is readily resolvable at the Fe K-edge. The 2-eV splitting of the pre-edge in all the complexes in Figure 13 can be attributed to this $^4F/^4P$ multiplet splitting. As in the ferric case, the pre-edge area of the five-coordinate high-spin ferrous model complex is greater than that of the six-coordinate complex (Figure 13c). However, the ferrous case is more complex since there are two pre-edge features which can have different intensity distributions. We are currently investigating the variation of this intensity distribution in a series of ferrous complexes.[91] Empirically the pre-edge of $[Fe^{II}PMA]^+$ solution and $Fe^{II}BLM$ look much more similar in shape and intensity to the six-coordinate ferrous complex. The pre-edge of $[Fe^{II}$-PMA$]^+$ solid has more intensity in the 7112-eV feature than in the higher energy feature, as does $[Fe(TMC)N_3]BF_4$, which is consistent with the MCD results of $[Fe^{II}PMA]^+$ solid being five-coordinate. However, the first pre-edge transition of $[Fe^{II}$-

(87) Shulman, R. G.; Yafet, Y.; Eisenberger, P.; Blumberg, W. E. *Proc. Natl. Acad. Sci. U.S.A.* **1976**, *73*, 1384−1388.
(88) Cramer, S. P.; Eccles, T. K.; Kutzler, F. W.; Hodgson, K. O.; Mortenson, L. E. *J. Am. Chem. Soc.* **1976**, *98*, 1287−1288.
(89) Roe, A. L.; Schneider, D. J.; Mayer, R. J.; Pyrz, J. W.; Widom, J.; Que, L., Jr. *J. Am. Chem. Soc.* **1984**, *106*, 1676−1681.
(90) Kau, L.-S.; Spira-Solomon, D. J.; Penner-Hahn, J. E.; Hodgson, K. O.; Solomon, E. I. *J. Am. Chem. Soc.* **1987**, *109*, 6433−6442.
(91) Westre, T. E.; Hedman, B.; Hodgson, K. O.; Solomon, E. I. To be submitted for publication.

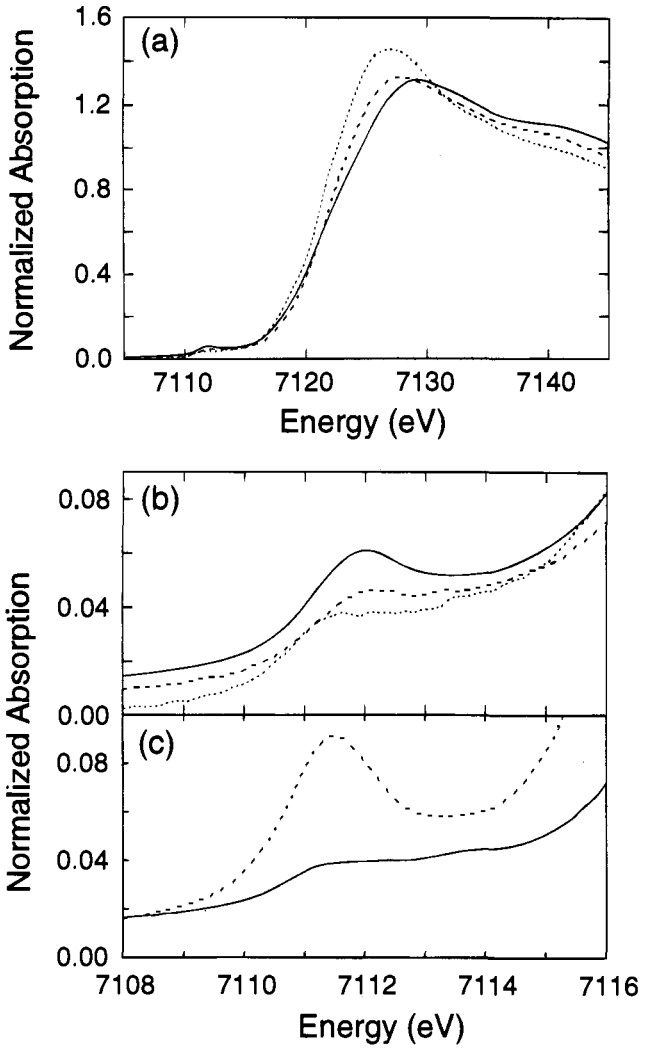

Figure 13. (a) Fe K XAS edge spectra of $[Fe^{II}PMA]^+$ solid (—), $[Fe^{II}PMA]^+$ solution (- - -), and $Fe^{II}BLM$ (• • •). (b) Expansion of the 1s → 3d pre-edge region of part a. (c) The 1s → 3d pre-edge region of a six-coordinate high-spin ferrous model complex $[Fe(imidazole)_6]Cl_2$ (—) and a five-coordinate complex $[Fe(TMC)N_3]BF_4$ (- - -).

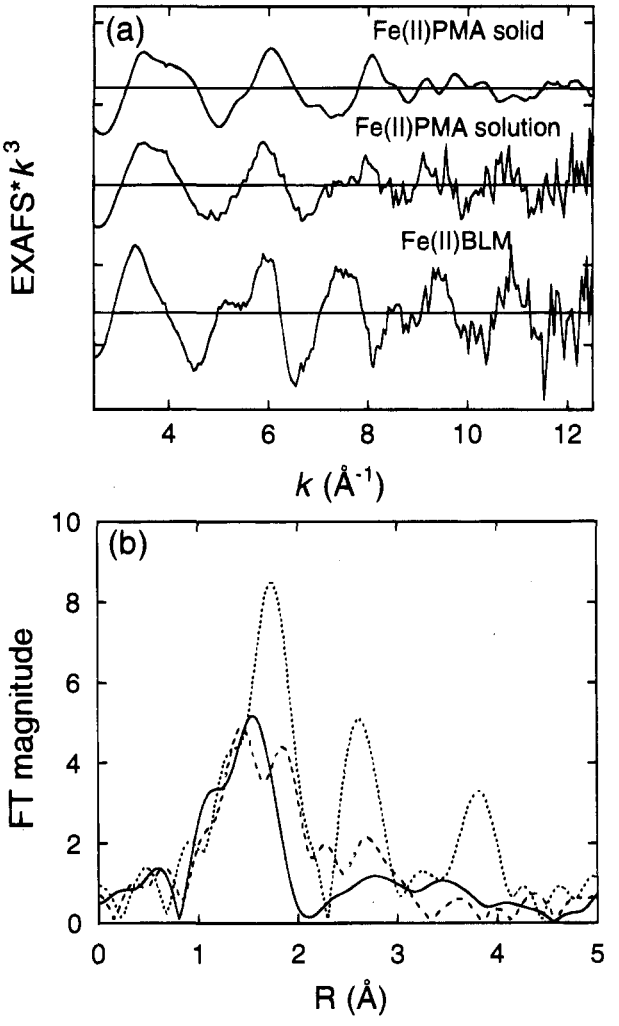

Figure 14. (a) EXAFS data ($*k^3$) for $[Fe^{II}PMA]^+$ solid, $[Fe^{II}PMA]^+$ solution, and $Fe^{II}BLM$ (the ordinate scale is 5 between major tick marks on an absolute scale from the abscissa with solid horizontal lines indicating the zero point of each plot). (b) The Fourier transforms (non-phase-shift corrected) over the k-range 3.5—12.5 Å^{-1} of the EXAFS data for $[Fe^{II}PMA]^+$ solid (—), $[Fe^{II}PMA]^+$ solution (- - -), and $Fe^{II}BLM$ (• • •).

PMA]$^+$ solid is not as intense as that of $[Fe(TMC)N_3]BF_4$. This could be due to the Fe $4p_z$ orbital of $[Fe^{II}PMA]^+$ solid mixing with the π^* orbital of the pyrimidine. This would diminish the intensity of the pre-edge feature since for square-pyramidal geometry the $4p_z$ orbital should be the dominant iron p-orbital mixing into the d-orbitals based on its lower energy[90] and the lack of inversion along the z-axis. This $4p_z$-pyrimidine π^* mixing would shift electric dipole intensity from the pre-edge into a higher energy region of the XAS spectrum.

EXAFS studies of $[Fe^{II}PMA]^+$ solid, $[Fe^{II}PMA]^+$ solution, and $Fe^{II}BLM$ were also pursued to obtain metrical information on the iron active site. The EXAFS spectra of $[Fe^{II}PMA]^+$ solid, $[Fe^{II}PMA]^+$ solution, and $Fe^{II}BLM$ are shown in Figure 14a and the Fourier transforms (FTs), taken over the k range of 3.5—12.5 Å^{-1}, are shown Figure 14b. Curve-fitting was performed on filtered first coordination shell contributions with FT backtransform windows given in Table 4 over the k range 4—12 Å^{-1} varying bond distances and coordination numbers. The results from the curve-fitting analysis are presented in Table 4. It should be noted that EXAFS analysis cannot readily distinguish between O and N coordination. However, given the likely ligation, only N parameters were used in the fits to the data. The EXAFS data of $[Fe^{II}PMA]^+$ solid could not be adequately fit with one shell of N atoms (Fit 1). The "goodness of fit parameter", F, was dramatically reduced when a second shell of N was added to the fit (Fit 2) giving N distances of 1.98 and 2.12 Å. However, the coordination number of 3.4 was still low and there was a mismatch in the fit to the data in the higher k region. Thus, a third shell of N was added to the fit (Fit 3). The F value was somewhat reduced and the fit matched the data more closely in the higher k region (Figure 15a), giving the best fit to the data with 1 N at 1.93 Å, 3 N at 2.07 Å, and 1 N at 2.23 Å. The $[Fe^{II}PMA]^+$ solution data also could not be fit adequately with a single shell of N (Fit 4). The F value dropped by a factor of 4 when a second shell of N was added (Fit 5), giving 2 N at 2.00 Å and 3 N at 2.17 Å. Inclusion of a third shell of N (Fit 6) did not substantially improve the fit (Figure 15b) and this contribution had a relatively low coordination number of 0.6. Thus, the physical significance of the contribution at 2.29 Å is more questionable. The $Fe^{II}BLM$ EXAFS data could be fit reasonably well with one shell of N at 2.16 Å (Fit 7). A two-shell fit (Fit 8) improved the F value and increased the coordination numbers. A three-shell fit was also tried (Fit 9); however, the fit to the data did not improve substantially (Figure 15c). The F value improved slightly and the total coordination number increased to 6.6 (*vs.* 4.4 for Fit 8). The outer-shell data of $Fe^{II}BLM$ will be further investigated, including multiple-scattering theory and software. Preliminary

Table 4. Summary of EXAFS Curve-Fitting Results

compd	fit no.	FT window width (Å)	CN[a,b]	element	bond length (Å)[b]	F
$[Fe^{II}PMA]^+$	1	0.8–2.1	1.5	N	2.04	0.53
solid	2	0.8–2.1	1.8	N	1.98	0.31
			1.6	N	2.12	
	3	0.8–2.1	1.3	N	1.93	0.25
			2.9	N	2.07	
			1.1	N	2.23	
$[Fe^{II}PMA]^+$	4	0.8–2.2	1.4	N	2.13	0.75
solution	5	0.8–2.2	2.0	N	2.00	0.17
			2.9	N	2.17	
	6	0.8–2.2	2.1	N	1.99	0.14
			3.3	N	2.15	
			0.6	N	2.29	
$Fe^{II}BLM$	7	1.0–2.25	3.0	N	2.16	0.41
	8	1.0–2.25	1.4	N	2.08	0.29
			3.0	N	2.19	
	9	1.0–2.25	1.6	N	2.06	0.23
			4.2	N	2.19	
			0.8	N	2.40	

[a] CN = coordination number. [b] Errors in distances (±0.02 Å) and coordination numbers (±25%) are estimated from the variance between EXAFS fitting results and values from models of crystallographically known structure.[59]

results indicate that the peak in the FT of the $Fe^{II}BLM$ data at ~2.6 Å in Figure 14b can be fit with Fe–N–C multiple-scattering.

The average first-shell distance of $[Fe^{II}PMA]^+$ in solution is ~0.1 Å longer than that of the $[Fe^{II}PMA]^+$ solid, consistent with the MCD and Fe K-edge data, which indicates that $[Fe^{II}PMA]^+$ solid is five-coordinate while $[Fe^{II}PMA]^+$ solution is six-coordinate. Both $[Fe^{II}PMA]^+$ solid and $[Fe^{II}PMA]^+$ solution have a first coordination sphere that has several contributions, as is evident from the curve-fitting results and the multiple peaks in the FTs (Figure 14b). $Fe^{II}BLM$ has a more regular first shell with an average first shell distance of 2.16 Å which is consistent with that of other six-coordinate high-spin ferrous complexes (2.16 ± 0.03 Å).[92–95] Importantly, a short Fe^{II}–N contribution is present in all three complexes, which increases in length along the series $[Fe^{II}PMA]^+$ solid (1.93 Å) < $[Fe^{II}PMA]^+$ solution (2.00 Å) < $Fe^{II}BLM$ (2.06–2.08 Å). This short N can reasonably be assigned to the pyrimidine based upon the high degree of covalency derived from the Abs, MCD, and rR results (*vide supra*). The trend in Fe–N_{Pm} distances correlates with the Fe K-edge energy positions and with differences in π-back-bonding as discussed below.

Discussion

With the array of data in the literature regarding the solution structure of $Fe^{II}BLM$, some controversy still remains as to the definitive metal-chelating mode of this ligand. We have addressed this problem by comparison to $[Fe^{II}PMA]^+$, which has been found by molecular modeling to be most stable with the pyrimidine, imidazole, deprotonated amide and secondary amine coordinated equatorially, and the primary amine bound axially, and it is thought to have a solvent molecule coordinated at the open site in solution.[96] Binding of solvent to the sixth site is confirmed from the ligand field MCD spectra of solid and solution $[Fe^{II}PMA]^+$. Solid $[Fe^{II}PMA]^+$ has a ^5E_g splitting of 6100 cm^{-1} indicating a five-coordinate, square-pyramidal structure (Figure 7a). On going to solution $[Fe^{II}PMA]^+$ the ^5E_g splitting decreases to 2110 cm^{-1}, indicating addition of a solvent molecule to the vacant axial position. The increase in coordination number is consistent with a decrease in the XAS pre-edge intensity as shown in Figure 13 and an increase in Fe–N bond lengths proceeding from five- to six-coordination as determined from the EXAFS analysis in Table 4. The similarities in the MCD ligand field spectrum and Δ^5E_g splitting of $Fe^{II}BLM$ (Figure 5) to that of the $[Fe^{II}PMA]^+$ in solution, as well as the comparable pre-edge shapes and intensities suggest that the coordination spheres of $Fe^{II}BLM$ and $[Fe^{II}PMA]^+$ in solution are not markedly different. The EXAFS analysis does indicate an overall increase in the Fe–N bond lengths of $Fe^{II}BLM$ relative to those of $[Fe^{II}PMA]^+$, which is consistent with the increased steric bulk of the BLM ligand compared with the more compact PMAH framework. Thus, a proposed solution structure of $Fe^{II}BLM$ is given in Figure 16 which is based on the PMAH ligand set and the experimental evidence that solvent coordinates at the sixth position. The steric constraints of the BLM ligand framework coupled with the labile coordination site occupied by the solvent molecule suggest that oxygen binding to the Fe^{2+}

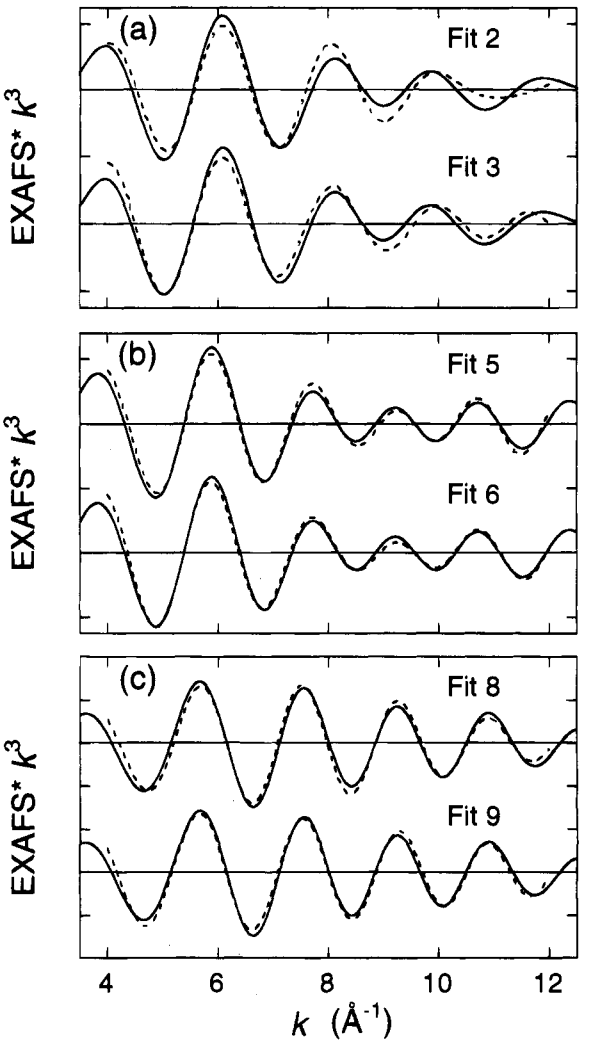

Figure 15. Empirical first-shell fits to the Fourier-filtered EXAFS data with the solid lines representing the experimental data and the dashed lines representing the fits to the data. (a) Fits 2 and 3 to the $[Fe^{II}PMA]^+$ solid data (Table 4). (b) Fits 5 and 6 to the $[Fe^{II}PMA]^+$ solution data. (c) Fits 8 and 9 to the $Fe^{II}BLM$ data. (The ordinate scale is 2 between consecutive tick marks with solid horizontal lines going through the zero point of each plot.)

(92) Montgomery, H.; Chastain, R. V.; Natt, J. J.; Witkowska, A. M.; Lingafelter, E. C. *Acta Crystallogr.* **1967**, *22*, 775–780.
(93) Price, D. C. *Can. J. Phys.* **1987**, *65*, 1280–1293.
(94) Miller, L. L.; Jacobsen, R. A.; Chen, Y.-S.; Kurtz, D. M., Jr. *Acta Crystallogr.* **1989**, *C45*, 527–529.
(95) Kitajima, N.; Fukui, H.; Moro-oka, Y. *J. Am. Chem. Soc.* **1990**, *112*, 6402–6403.
(96) Wu, Y.-D.; Houk, K. N.; Valentine, J. S.; Nam, W. *Inorg. Chem.* **1992**, *31*, 718–720.

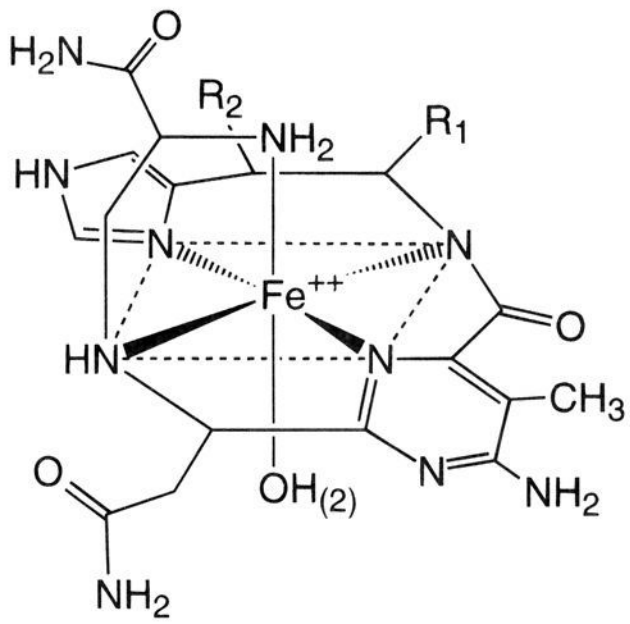

Figure 16. Proposed solution structure of $Fe^{II}BLM$. R_1 is the linker moiety, bithiazole tail, and terminal amine. R_2 is the mannose sugar moiety.

center occurs via a dissociative mechanism. This is supported by the fact that in solution the Δ^5E_g splitting in the room temperature CD spectrum of $Fe^{II}BLM$ increases to $\sim$3600 cm^{-1}, indicating that an axial ligand, likely H_2O or OH^-, in $Fe^{II}BLM$ is weakly coordinated to the iron. Our spectral studies of solid $[Fe^{II}PMA]^+$ have defined the five-coordinate complex as being square pyramidal, which produces an open coordination position available for O_2 reaction. On the basis of the similarity in spectral features and activation chemistry of $[Fe^{II}PMA]^+$ and $Fe^{II}BLM$ in solution, this square-pyramidal structure is reasonably correlated with the reactive intermediate in the mechanism of O_2 binding to $Fe^{II}BLM$.

In addition to the geometric structure obtained for $Fe^{II}BLM$ through the MCD excited state ligand field and XAS analyses, the electronic structures of $Fe^{II}BLM$ and $[Fe^{II}PMA]^+$ have been elucidated through MCD ligand field ground state, charge transfer excited state, and rR spectroscopies. From the ligand field analysis, $[Fe^{II}PMA]^+$ solid exhibits nested saturation magnetization curves (Figure 6b) consistent with the five-coordinate, square-pyramidal geometry. The value of $V/2\Delta$ (0.33) derived from this analysis indicates that the structure is highly rhombic due to the short Fe−N bond distance in the equatorial plane determined from the EXAFS results which supports the presence of strong metal−ligand π-backbonding. In solution $[Fe^{II}PMA]^+$ and $Fe^{II}BLM$ also exhibit nested saturation magnetization curves that result in unusually small values of the spin Hamiltonian parameter δ in Figure 2, not generally observed for six-coordinate non-heme ferrous active sites. This corresponds to a large splitting of the t_{2g} set of d-orbitals ($-\Delta$) which requires strong π-bonding interaction between the metal and pyrimidine π^* orbitals. The values of $V/2\Delta$ of 0.24 for $[Fe^{II}PMA]^+$ and 0.18 for $Fe^{II}BLM$ indicate a more moderate degree of rhombic distortion which decreases with increasing Fe−N bond length. Thus the magnitudes of δ (and $-\Delta$) are different from typical six-coordinate model complexes indicating that strong π-bonding effects are present, consistent with the EXAFS results exhibiting a short Fe−N distance.

An important deviation from non-heme ferrous behavior demonstrated by $Fe^{II}BLM$ and $[Fe^{II}PMA]^+$ is the existence of low-energy CT transitions analogous to $d_\pi \rightarrow \pi^*$ MLCT transitions in heme systems.[97] Assignment of these bands as iron(II) → pyrimidine MLCT transitions derives from the shift

(97) Lever, A. B. P.; Gray, H. B. *Iron Porphyrins: Part One*; Addison-Wesley Publishing Co., Inc.: Reading, 1983.

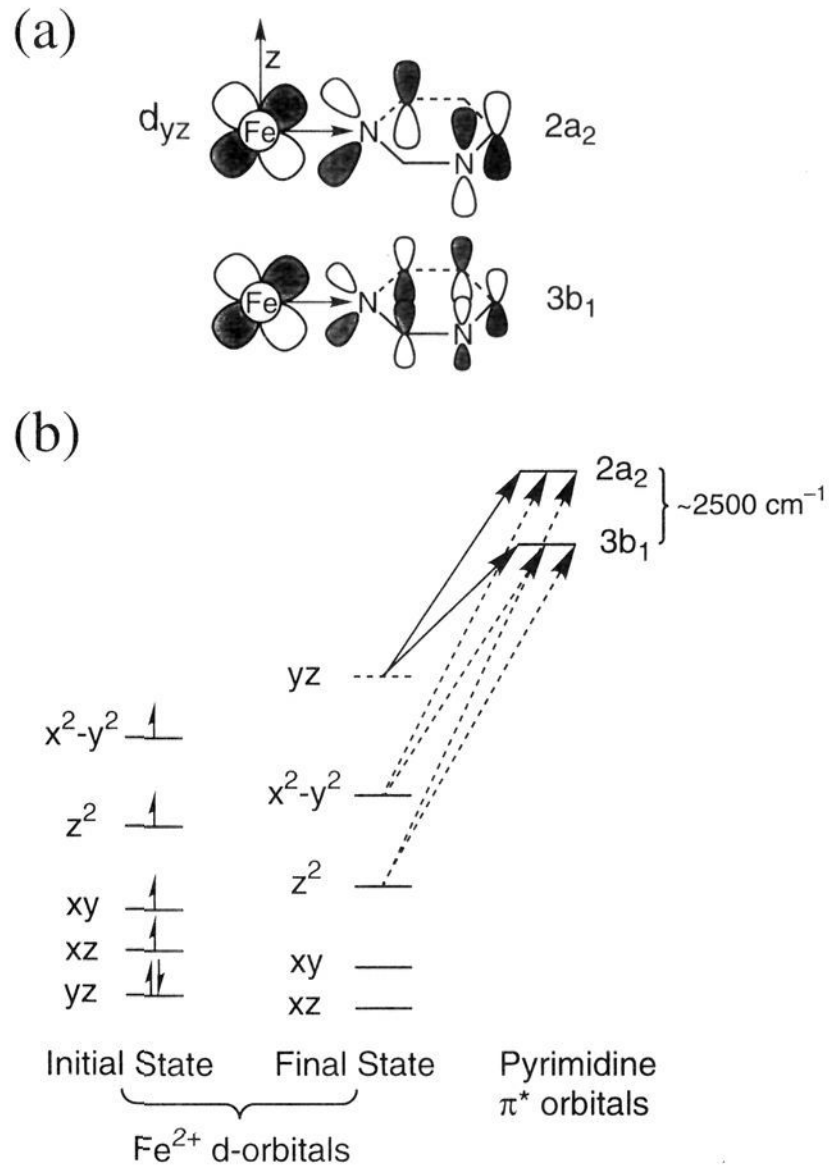

Figure 17. (a) Molecular coordinate scheme and nodal pattern for the Fe^{2+} d_{yz} orbital π-bonding to the pyrimidine $2a_2$ and $3b_1$ (π^*) orbitals. The $2a_2$ (π^*) pyrimidine orbital has a larger coefficient on the coordinated nitrogen atom than the $3b_1$ (π^*) orbital which is indicated by the difference in the size of the lobes. (b) Molecular orbital energy level diagram for $Fe^{II}BLM$ and $[Fe^{II}PMA]^+$ depicting the initial and final state Fe^{2+} d-orbital energies prior to and upon metal-to-ligand charge transfer, respectively, to the pyrimidine $2a_2$ and $3b_1$ (π^*) orbitals which are split by 2000−3000 cm^{-1}. The final state order includes the loss of electron repulsion energy on the d_{yz} orbital. The predicted metal-to-ligand charge transfer transitions, based on overlap and symmetry considerations, are identified with solid arrows for the intense transitions and dashed arrows for the weaker transitions.

in the CT Abs spectra of the structurally perturbed analogs of $[Fe^{II}PMA]^+$ (Figure 10) as well as the strong resonance enhancement of virtually all pyrimidine normal modes observed in the Raman spectrum of $[Fe^{II}PMA]^+$ (Figure 12). However, a more rigorous spectroscopic assignment that accounts for the presence of at least five CT bands derives from consideration of Fe and pyrimidine molecular orbital (MO) interactions. Of the three pyrimidine π^* orbitals, the totally antisymmetric linear combination is high in energy relative to the lower lying $3b_1$ (π^*) and $2a_2$ (π^*) orbitals.[98,99] As shown in Figure 17, the $2a_2$ (π^*) orbital lies higher in energy by $\sim$2000−3000 cm^{-1}.[100−102] For both π^* orbitals, a lobe exists on the nitrogen coordinated to the Fe^{2+} center perpendicular to the pyrimidine plane which can have sufficient overlap with d-orbitals of the appropriate symmetry resulting in MLCT transitions, the intensity of which

(98) Tabner, B. J.; Yandle, J. R. *J. Chem. Soc. A, Inorg. Phys. Theor.* **1968**, 381−388.
(99) Innes, K. K.; Ross, I. G.; Moomaw, W. R. *J. Mol. Spectrosc.* **1988**, *132*, 492−544.
(100) Benedix, R.; Hennig, H. *J. Prakt. Chem.* **1984**, *326*, 962−970.
(101) Jaffe, H. H.; Orchin, M. *Theory and Applications of Ultraviolet Spectroscopy*; John Wiley & Sons, Inc.: New York, 1962.
(102) Lavallee, D. K.; Fleischer, E. B. *J. Am. Chem. Soc.* **1972**, *94*, 2583−2599.

is proportional to the degree of overlap between the donor and acceptor orbitals involved in the CT transition. The greater the Fe^{2+} d_π and pyrimidine π^* orbital overlap, the greater the intensity of the MLCT transition. The coefficient of the pyrimidine π^* wave functions localized at the nitrogen bonded to the iron is larger for the $2a_2$ (π^*) orbital than for the $3b_1$ (π^*) orbital indicating transitions to the higher energy $2a_2$ π^* orbital should be more intense.[103,104] With the weak molecular z-axis of Fe^{II}BLM (and $[Fe^{II}PMA]^+$) defined as the primary amine−solvent direction and the equatorial pyrimidine ligand as the y-axis (Figure 17a), the Fe d_{yz} orbital has the greatest overlap with the pyrimidine π^* MOs and is also of the appropriate symmetry (A′ in a C_s point group with the yz-plane defined as the symmetry element) for these MOs to interact. Therefore, two Fe d_{yz} → pyrimidine π^* CT transitions are expected which will be split in energy by ~2000−3000 cm^{-1} with the higher energy transition to the $2a_2$ MO having the greater intensity. In addition, both the $d_{x^2-y^2}$ and d_{z^2} orbitals are of the same symmetry as the d_{yz} orbital and can undergo configuration interaction which shifts some intensity into CT transitions from these d-orbitals to the pyrimidine π^* orbitals. The d_{yz} orbital should be lowest in energy, as shown in the initial state bonding diagram depicted in Figure 17b, due to its strong π-bonding interaction with the pyrimidine π^* levels and thus should contain the extra electron of the d^6 configuration. Its transition energy, however, will go down relative to those from other Fe d-orbitals due to the loss of electron repulsion in the transition. Thus the actual energy of transitions from the d-orbitals to the pyrimidine π^* levels will be dependent upon the energies of the two π^* orbitals, the initial d-orbital energies, and the loss of electron repulsion from the d_{yz} orbital which will be large, resulting in the approximate final state energy diagram in the center of Figure 17b. Thus, the pattern predicted for the lowest energy spin allowed CT transitions (Figure 17) has the lowest two energy bands Fe d_{yz} → pyrimidine π^* $3b_1$ and $2a_2$ split by the energy gap of the π^* orbitals (~2000−3000 cm^{-1}) with the higher energy transition of the two having the greater intensity, followed by four less intense transitions to higher energy, dependent on the initial splittings of the d-orbitals and the loss of electron repulsion. This energy and intensity pattern has a reasonable correlation with Bands 1−5 observed in the Abs and MCD spectra of Fe^{II}BLM and $[Fe^{II}PMA]^+$ shown in Figures 8 and 9. At least five bands are required to fit the experimental data; however, a similar fit would be obtained by including a sixth transition within this region. Although the MLCT energies and intensities of Bands 1−5 show agreement with the qualitative bonding model illustrated in Figure 17, rigorous assignment of these transitions requires quantitation of final state relaxation effects through transition state electronic structure calculations (currently underway).

Since the low-energy Abs and MCD bands in Fe^{II}BLM and $[Fe^{II}PMA]^+$ originate from iron(II) → pyrimidine MLCT transitions their intensities and energies serve to probe the degree of metal-to-ligand π-backbonding. This bonding interaction derives from the mixing of metal d- and pyrimidine π^* molecular orbitals, the wave function of which can be expressed as a linear combination of these orbitals (Fe and Pm) with normalized coefficients of mixing: $\Psi = C_{\pi M}Fe + C_{\pi L}Pm$. The intensity of a given CT transition has been shown to be proportional to the magnitude of the coefficient ($C_{\pi L}^2$) of the ligand in the metal-derived MO.[105,106] The greater intensity of the $[Fe^{II}PMA]^+$ MLCT transition in the Abs spectrum relative to that of Fe^{II}BLM (ϵ_{670} = 1850 M^{-1} cm^{-1} and ϵ_{476} = 380 M^{-1} cm^{-1}, respectively) indicates a larger value of $C_{\pi L}^2$ and hence a greater degree of π-backbonding in $[Fe^{II}PMA]^+$. In addition to the decrease in intensity, the MLCT bands in the Abs and MCD spectra of $[Fe^{II}PMA]^+$ shift in energy on going from the solid (~15 000 cm^{-1}) to solution (~18 000 cm^{-1}) and this trend continues for Fe^{II}BLM (~20 000 cm^{-1}). The energies of MLCT transitions are dependent on coordination number and considering only the effects of repulsive ligand interactions on the d-orbitals would be expected to blue shift when a ligand is removed from the iron center. However, as the coordination number decreases, metal−ligand bonding becomes more covalent, which raises the energy of the predominantly antibonding donor orbital on the metal, inducing a shift to lower energy of the CT transition as is observed in the Abs and MCD spectra of the five-coordinate $[Fe^{II}PMA]^+$ solid relative to the six-coordinate species in solution. The difference in the CT energies between Fe^{II}BLM and $[Fe^{II}PMA]^+$ in solution directly results from the electron donating or withdrawing nature of the substituents on the pyrimidine ring as they either raise or lower the energy of the π^* orbitals of the pyrimidine ligand.[107,108] Specifically, based on Hammett σ substituent constants, replacement of the electron donating NH_2 group and the electronically inert CH_3 group on the pyrimidine ring in Fe^{II}BLM with the moderately electron withdrawing Br atom in $[Fe^{II}PMA]^+$ results in a substantial red shift of the MLCT envelope of ~6100 cm^{-1}. Comparable shifts have also been observed for MLCT transitions in para-substituted pyridine (L) complexes of $[(CN)_5Fe^{II}(L)]^{3-}$ following similar substitution.[109] The importance of the electron donating ability of the NH_2 group cannot be underestimated as replacement of a hydrogen atom with Br in $[Fe^{II}(Prpep)_2]$ induces a red shift in the MLCT band centered at 670 nm of only 650 cm^{-1}, thus suggesting that the NH_2 group plays a large role in raising the energy of the MLCT state and thus affecting the pyrimidine−Fe(II) bond (*vide infra*). The strong blue shift in the CT band energies is responsible for the reduced intensity of the transitions since the intensity is directly proportional to $C_{\pi L}$ (*vide supra*) which is given by the following: $C_{\pi L} \approx H_{d_\pi}/\Delta E$, where H_{d_π} is the resonance integral proportional to overlap and ΔE is the difference in energy between the d_{yz} and pyrimidine π^* orbitals and thus approximates the CT energy. Therefore, the lower energy, higher intensity CT transitions of $[Fe^{II}PMA]^+$ in solution relative to Fe^{II}BLM demonstrate a greater $C_{\pi L}$ and hence degree of metal−ligand π-backbonding between the d-orbitals of Fe^{2+} and the pyrimidine π^* orbitals. The still lower energy of the MLCT bands for solid $[Fe^{II}PMA]^+$ indicates enhanced π-backbonding in the five-coordinate structure. This trends parallels the decrease in Fe−N_{Pm} bond lengths determined from the EXAFS analysis.

These MLCT transitions in Fe^{II}BLM and $[Fe^{II}PMA]^+$ indicate the presence of significant π-backbonding not observed for other non-heme iron centers. This results from the presence of five strong field nitrogen ligands (with solvent occupying the sixth site) complexed to the Fe^{2+} which raises the energy of the d-manifold, reduces the energy gap between the d_π and ligand

(103) Nagaoka, S.-i.; Nagashima, U. *J. Phys. Chem.* **1990**, *94*, 4467−4469.
(104) Benedix, R.; Hennig, H. *Z. Anorg. Allg. Chem.* **1989**, *577*, 23−28.
(105) Baldwin, M. J.; Root, D. E.; Pate, J. E.; Fujisawa, K.; Kitajima, N.; Solomon, E. I. *J. Am. Chem. Soc.* **1992**, *114*, 10421−10431.
(106) Solomon, E. I.; Tuczek, F.; Root, D. E.; Brown, C. A. *Chem. Rev.* **1994**, *94*, 827−856.
(107) Toma, H. E.; Malin, J. M. *Inorg. Chem.* **1973**, *12*, 1039−1045.
(108) Hine, J. *Physical Organic Chemistry*, 2nd ed.; McGraw-Hill Book Company, Inc.: New York, 1962.
(109) Johnson, C. R.; Shepherd, R. E. *Inorg. Chem.* **1983**, *22*, 2439−2444.

π^* orbitals, and increases the propensity for metal−ligand backbonding at the site. This π-backbonding contributes to the unique chemistry and reactivity of $Fe^{II}BLM$. Unlike other non-heme iron active sites, $Fe^{II}BLM$ reversibly binds CO and reacts with NO and other strong field ligands to form low-spin complexes. Addition of this sixth strong field ligand induces the low-spin conversion through an increase in the already sizable splitting (*i.e.*, all nitrogen ligands) of the d-orbitals ($10Dq$) which overcomes the electron-spin pairing energy. The unusual binding of CO derives from the tendency of the Fe^{II}-BLM site to backbond. Similar "symbiotic" behavior is common in inorganic coordination complexes and is rationalized by the relative softness (*i.e.*, polarizability) of the metal center induced by the coordination sphere.[110] Formation of the Fe^{II}-BLM−CO complex is further promoted by the increased ligand field stabilization energy of the resultant low-spin d^6 configuration. The presence of backbonding also contributes to the unusual O_2 reactivity of this site relative to other non-heme Fe systems. Backbonding to the pyrimidine ligand decreases the extent of charge transfer to the O_2 which shifts the equilibrium in eq 2 to the left, making FeBLM less likely to dissociate O_2^- and contributing to the reversible binding of O_2 by the site.

$$Fe^{2+} + O_2 \rightleftharpoons Fe^{3+}-O_2^- \rightleftharpoons Fe^{3+} + O_2^- \qquad (2)$$

This reduced charge transfer to the bound superoxide also enhances its propensity for further reduction to form the $Fe^{III}-O_2^{2-}$ site of activated BLM. This is in contrast to a pathway observed in other non-heme iron systems where strong π-backbonding is absent. In these cases, a diffusable superoxide radical may be formed by direct autoxidation of the Fe^{2+} site (eq 2, right).[111,112] In the presence of DNA, a superoxide radical would lead to non-selective cleavage products which are not observed in BLM chemistry.[10]

The low-energy MLCT transitions, the reversible binding of O_2, and the formation of low-spin complexes with CO and NO suggest that $Fe^{II}BLM$ more closely parallels heme rather than non-heme iron chemistry. Yet the differences in these ferrous centers are significant as heme systems exhibit more intense ($\epsilon \approx 10\,000\ M^{-1}\ cm^{-1}$), lower energy ($\sim 10\,000\ cm^{-1}$) MLCT transitions than $Fe^{II}BLM$ indicating much greater Fe^{2+} backbonding into the tetrapyrrole macrocycle.[97] This difference in backbonding correlates with differences in the O_2 reactivity of BLM relative to heme iron centers. In particular, the oxygen intermediate of cytochrome P-450 is thought to be a ferryl species[26,113] which is structurally distinct from the peroxide-level intermediate of activated BLM.[27,28] Our results suggest that other non-heme Fe enzymes which exhibit little or no low-energy MLCT transitions relative to $Fe^{II}BLM$ may be expected to form intermediates which more closely resemble the ferric-peroxide species of activated BLM than the ferryl species of heme systems.

In summary, our studies have provided significant insight into the oxygen reactivity of $Fe^{II}BLM$. The lability of high-spin iron combined with steric constraints of the BLM ligand framework and its weaker axial interaction with solvent support a dissociative mechanism for O_2 reactivity. Our spectroscopic studies of solid $[Fe^{II}PMA]^+$ have defined the nature of such a five-coordinate intermediate as square pyramidal which provides an open coordination position for reaction with O_2. A major electronic structure difference between $Fe^{II}BLM$ (and $[Fe^{II}$-$PMA]^+$) and other non-heme ferrous sites is the presence of low-energy CT transitions which reflect strong iron(II) → pyrimidine backbonding. Relative to non-heme iron complexes this backbonding results in reduced charge donation to the O_2 which (1) contributes to the reversible binding of O_2 exhibited by $Fe^{II}BLM$, (2) stabilizes the initial $Fe^{III}-O_2^-$ intermediate from loss of O_2^- and reaction with substrate, and (3) promotes the further reduction of $Fe^{III}BLM-O_2^-$ to form activated BLM. Despite generally being considered a non-heme iron system due to the absence of an extensive delocalized π network, the existence of low-energy MLCT transitions with reasonable intensity, hence the presence of some backbonding, identifies BLM as an important link bridging the chemistry of non-heme and heme active sites.

Acknowledgment. We gratefully acknowledge Mark Pavlosky for his scientific contributions to this study. This work was supported by grants from the National Institutes of Health (GM40392, E.I.S.), National Science Foundation (CHE-9121576, K.O.H.), National Cancer Institute (CA 53076, P.K.M.), and American Cancer Society (CH-481, P.K.M.). SSRL is supported by the US Department of Energy, Office of Basic Energy Science, Divisions of Chemical and Materials Sciences, and in part by the National Institutes of Health, Biomedical Research Technology Program (RR-01209, K.O.H.), and the US Department of Energy, Office of Health and Environmental Research. J.M.Z. thanks the Jane Coffin Childs Fund for Medical Research for a postdoctoral fellowship. R.J.G. was supported by a NIH-MBRS grant (GM08132).

JA943513C

(110) Jørgensen, C. K. *Inorg. Chem.* **1964**, *3*, 1201−1202.
(111) Feig, A. L.; Lippard, S. J. *Chem. Rev.* **1994**, *94*, 759−805.
(112) Brown, E. R.; Mazzarella, J. D. *J. Electroanal. Chem.* **1987**, *222*, 173−192.
(113) Dawson, J. H. *Science* **1988**, *240*, 433−439.